HAL open science

High resolution adaptive framework for fast transient fluid-structure interaction with interfaces and structural failure Application to failing tanks under impact

V. Faucher, F. Casadei, F. Larcher, G. Valsamos

▶ **To cite this version:**

V. Faucher, F. Casadei, F. Larcher, G. Valsamos. High resolution adaptive framework for fast transient fluid-structure interaction with interfaces and structural failure Application to failing tanks under impact. International Journal of Impact Engineering, 2018, 10.1016/j.ijimpeng.2018.10.008 . cea-02339946

HAL Id: cea-02339946

https://cea.hal.science/cea-02339946v1

Submitted on 21 Oct 2021

HAL is a multi-disciplinary open access archive for the deposit and dissemination of scientific research documents, whether they are published or not. The documents may come from teaching and research institutions in France or abroad, or from public or private research centers.

L'archive ouverte pluridisciplinaire **HAL**, est destinée au dépôt et à la diffusion de documents scientifiques de niveau recherche, publiés ou non, émanant des établissements d'enseignement et de recherche français ou étrangers, des laboratoires publics ou privés.

Distributed under a Creative Commons Attribution - NonCommercial 4.0 International License

Version of Record: https://www.sciencedirect.com/science/article/pii/S0734743X18301726
Manuscript_456f427dfde0cb288291ea56af4193f3

High resolution adaptive framework for fast transient fluid-structure interaction with interfaces and structural failure – Application to failing tanks under impact

Vincent Faucher[a*], Folco Casadei[b], Georgios Valsamos[b], Martin Larcher[b]

[a] *CEA, DEN, CAD, DTN, Dir, Saint-Paul-les-Durance, France, F-13108*

[b] *European Commission, Joint Research Centre (JRC), Directorate for Space and Migration, Safety and Security of Buildings Unit, 21027 Ispra, Italy*

[*] *Corresponding author*

Nomenclature

See Table 1.

1. Context and outline

The present paper is dedicated to the simulation of fast transient phenomena involving multicomponent flows (mainly liquid-gas flows in the present case, but reactive flows like combustion fronts could be considered with the same approach) and fluid-structure interaction.

A comprehensive bibliography is available on such topics, from the resistance of structures to underwater explosions (see for instance Schiffer and Tagarielli, 2015 or Barras et al., 2012) to slamming problems for marine engineering, involving impacts of structures on free liquid surfaces (see Panciroli et al., 2015 or Van Nuffel et al., 2013 among many others) or sloshing liquid inside tanks under dynamic loading (see Nicolici et al., 2013, or Brar and Singh, 2014). These situations are generally characterized by finite structural motions, fluid interfaces interacting with structures and strong inertial coupling between liquid(s) and structures, orienting the choice of the suitable numerical framework to implement for their accurate simulations. A specific difficulty is added when the structure is allowed to undergo failure and fragmentation, due to the specificities of crack initiation and propagation on the one hand, and to the magnification of the influence of fluid-structure interaction during the failing process on the other hand.

The main objective of the current paper is to design a generic, robust and highly accurate computational strategy able to handle all the features introduced above, with the intention of providing a significant improvement in the resolution of local phenomena, which can prove of primary importance for the global dynamic response of the system and for the evaluation of the potential consequences on its surrounding environment. Although the paper does not address a specific physical situation, the case of failing tanks under impact is considered to efficiently validate and challenge the proposed framework, since it includes all aforementioned relevant phenomena (i.e. impact and fast transient dynamics, liquid-gas interfaces and structural failure). A significant corresponding integral experiment is available for use by the authors (see Caleyron et al, 2013 for previous work describing the test configuration and exploiting some results). Moreover, in addition to the structural analysis of the tank during and after impact, characterizing the leaking liquid jet is a topic of great interest for many industries (nuclear for instance, see Jeon et al., 2012 or Lin and Tang, 2017), especially since 2001/9/11 with the major consequences on buildings due to the fire consecutive to fuel projections during the crash. Such simulations are likely to greatly benefit from the increase of resolution in fluid-structure interface tracking demonstraded in this paper.

© 2018 published by Elsevier. This manuscript is made available under the CC BY NC user license
https://creativecommons.org/licenses/by-nc/4.0/

To achieve the stated objectives, the proposed research first relies on state-of-the-art approaches recently published by the authors and co-workers, one for every specific physical feature involved in the coupled fluid-structure system (see Faucher 2014, Aune et al. 2016, Faucher et al., 2017). Then, the major improvement brought by the current paper is their combination into a generic multi-purpose adaptive framework providing the expected high resolution level in the simulation process. One major concern addressed by the authors is the full compatibility of the built strategy with models of industrial complexity, which requires the handling of fully unstructured meshes for fluids and structures, including plates and shells, and the design of a new class of unified refinement indicators, to be computed and combined with the required versatility and efficiency.

The paper is organized as follows. In the second section, the general computational framework is recalled, in terms of equations of motion, equations of state for fluids, constitutive laws for structures and modelling of multi-component flows with accurate interface management. For the sake of clarity and with minor loss of generality with respect to the industrial context expressed above, we focus on water-air flows involved in the applicative part of the paper. The third section is then specifically dedicated to the proposed multi-purpose mesh adaptation strategy with new combined refinement indicators for fluids and structures.

The fourth and fifth sections are finally devoted to challenging the introduced framework against the integral experiment mentioned above, with a two steps path. First, a parametric analysis is carried out in the fourth section on a simple, yet significant, simplified test case implementing all the physical features from the complex target case. This is is designed to bring some valuable knowledge on the global behavior of the new computational strategy, to discriminate between the various improvements brought by combined refinement indicators and to set the relevant paradigms, in terms of liquid-gas interface representation and of refinement levels for both fluid and structure, to be implemented in the simulation of the realistic experimental configuration. The corresponding calculations are then provided in the fifth section, along with the representative comparisons between numerical results and experimental data.

2. Basic equations for transient fluid-structure dynamics with water-air flows

We quickly recall in this section the basic equations governing the evolution of the fluid-structure systems considered throughout the current paper. As already stated in the introduction, they result from a series of recently published articles to which the reader is advised to refer for specific details. Table 1 gathers the descriptions of the variables used in Sections 2.1 and 2.2.

2.1 Equations of motion and EOS

The generic set of Euler equations governing the evolution of the systems considered in the present article reads, in Eulerian or *Arbitrary Lagrangian Eulerian* (ALE) representation for the fluid (see Donea et al., 2004) and Lagrangian representation for the structure:

$$\frac{\partial \rho}{\partial t} + \mathrm{div}\left(\rho \mathbf{u}\right) = 0 \quad \text{(total fluid mass conservation)} \tag{1-a}$$

$$\frac{\partial \rho \mathbf{u}}{\partial t} + \rho \mathbf{u} \cdot \nabla \mathbf{u} + \nabla P + \mathbf{f}_{S \to F} = \mathbf{f}_{vol}^{F} \text{ (total fluid momentum conservation)} \tag{1-b}$$

$$\frac{\partial \rho E}{\partial t} + \mathrm{div}\left[(\rho E + P)\mathbf{u}\right] = 0 \text{ (total fluid energy conservation)} \tag{1-c}$$

$$\rho \frac{\partial^2 \mathbf{q}}{\partial t^2} + \mathrm{div}\left[\boldsymbol{\sigma}(\boldsymbol{\varepsilon})\right] + \mathbf{f}_{F \to S} = \mathbf{f}_{vol}^{S} \text{ (structural equilibrium)} \tag{1-d}$$

For structures, the relation between the stress tensor and the strain tensor is non-linear in general, with many material constitutive laws, from simple elasticity to plasticity and damage.

Water-air flows are represented using a multi-component formalism (mixture model) coming with an additional set of equations written below in the case of stiffened gas EOS used for both components (see for instance Harlow and Amsden, 1971 and Le Metayer et al., 2003). The capability of such a model for the fluid to accurately reproduce relevant phenomena for transient fluid-structure interactions is demonstrated in (Faucher et al., 2017).

$$P_i = (\gamma_i - 1)\rho_i(e_i - q_i) - \gamma_i P_i^{\infty} \text{ (EOS for both components, i=1,2)} \tag{2-a}$$

$$\frac{\partial \rho c_1}{\partial t} + \mathrm{div}(\rho c_1 \mathbf{u}) = 0 \text{ (mass conservation for component 1)} \tag{2-b}$$

$$\frac{\partial \alpha_1}{\partial t} + \mathbf{u} \cdot \nabla \alpha_1 = 0 \text{ (non-conservative volumetric fraction transport for component 1)} \tag{2-c}$$

$$P_1(\rho_1, e_1) = P_2(\rho_2, e_2) \text{ (isobaric closure)} \tag{2-d}$$

The main variables for the description of the mixture are the volume fractions α_i and mass fractions c_i for each component. The following relations hold:

$$\begin{aligned} &\alpha_1 + \alpha_2 = 1 \\ &\rho_i = \frac{c_i \rho}{\alpha_i} \end{aligned} \tag{3}$$

With volumetric fractions known from the non-conservative transport equation and mass fractions known from the mass conservation equations (both total and for component 1), per-component densities can be computed from Equations (3). The isobaric closure is then used to compute directly the equilibrium pressure in the mixture through the following procedure:

$$\rho_i e_i = \frac{P + \gamma_i P_i^{\infty}}{\gamma_i - 1} + \gamma_i q_i \text{ (per-component specific energies computation)} \tag{4-a}$$

$$\rho e = \sum_{i=1,2} \alpha_i \left(\frac{P + \gamma_i P_i^{\infty}}{\gamma_i - 1} + \gamma_i q_i \right) = \rho E - \frac{1}{2}\rho \mathbf{u}^2 \text{ (total energy computation)} \tag{4-b}$$

$$P = \frac{\rho E - \frac{1}{2}\rho \mathbf{u}^2 - \sum_{i=1,2}\left(\frac{\alpha_i \gamma_i P_i^{\infty}}{\gamma_i - 1} + \alpha_i \gamma_i q_i\right)}{\sum_{i=1,2}\frac{\alpha_i}{\gamma_i - 1}} \quad \text{(pressure computation)} \tag{4-c}$$

It must be noticed that fast transient phenomena involving liquids often come with phase change effects (cavitation for instance, see Deletombe et al., 2017 for such a situation with hydrodynamic ram). Fortunately, basic stiffened gas Equations Of State can classically be extended with such features (see for instance Chiapolino et al., 2017). However, it represents an active research field in physics, beyond the scope of the current paper focusing on the coupled resolution process, which remains unaffected by evolutions brought to local constitutive models.

As the proposed validation tests do not yield high levels of tensile stress in liquids, a simple lower limitation of the pressure to the saturation pressure is enough to ensure the stability of the resolution process and mimic the local effects of cavitation with no significant effect on the global physical solution.

2.2 Time and space discretization

Space is discretized through Finite Elements for the structure and via a hybrid Finite Element/Finite Volume method for the fluid. More specifically, the mass and energy conservation equations, as well as the volume fraction transport equation for the stiffened gas combination, are treated with a Finite Volume procedure. On the contrary, the total momentum conservation equation is approximated with a non-conservative Finite Element scheme, presenting two advantages in the present situation:

1. the fluid kinematic variables are located at the nodes of the fluid grid and have the same nature as the structural kinematic quantities, providing a simple framework to impose link conditions between the two entities,
2. the velocity field in the fluid is obtained independently from the other conservation equations, which simplifies the implementation of a Lagrange-Remap approach, required by the VOFIRE anti-dissipative scheme for the *a posteriori* accurate localization of the water-air interfaces (see Després et al., 2010 ; Faucher and Kokh, 2013 ; Faucher et al., 2017).

Time integration is carried out through the central difference explicit scheme for the structure and through an explicit forward Euler scheme between mid-steps for the fluid. From time step *n* to time step *n+1*, it writes:

$$\begin{aligned}
&\dot{\mathbf{q}} = \frac{\partial \mathbf{q}}{\partial t}\,;\ \ddot{\mathbf{q}} = \frac{\partial^2 \mathbf{q}}{\partial t^2}\,;\ \dot{\mathbf{u}} = \frac{\partial \mathbf{u}}{\partial t}\\
&\dot{\mathbf{q}}^{n+1/2} = \dot{\mathbf{q}}^{n} + \frac{\Delta t}{2}\ddot{\mathbf{q}}^{n}\\
&\mathbf{q}^{n+1} = \mathbf{q}^{n} + \Delta t\,\dot{\mathbf{q}}^{n+1/2}\\
&\dot{\mathbf{q}}^{n+1} = \dot{\mathbf{q}}^{n+1/2} + \frac{\Delta t}{2}\ddot{\mathbf{q}}^{n+1}\\
&\mathbf{u}^{n+1/2} = \mathbf{u}^{n} + \frac{\Delta t}{2}\dot{\mathbf{u}}^{n}\\
&\mathbf{u}^{n+1} = \mathbf{u}^{n+1/2} + \frac{\Delta t}{2}\dot{\mathbf{u}}^{n+1}
\end{aligned} \tag{5}$$

This yields the linear system to solve at each time step to compute the accelerations for fluid and structure, completed by the balance of mass, energy and volume fraction (optionally) inside the fluid finite volumes:

$$
\begin{aligned}
&\begin{bmatrix} \mathbf{M}_F^{n+1} & \\ & \mathbf{M}_S \end{bmatrix} \begin{bmatrix} \dot{\mathbf{U}}^{n+1} \\ \ddot{\mathbf{Q}}^{n+1} \end{bmatrix} + \begin{bmatrix} {}^T\mathbf{N}_F^{n+1} \\ {}^T\mathbf{N}_S^{n+1} \end{bmatrix} \mathbf{\Lambda}^{n+1} = \begin{bmatrix} \mathbf{F}_F^{n+1} \\ \mathbf{F}_S^{n+1} \end{bmatrix} \\
&\mathbf{N}_F^{n+1}\dot{\mathbf{U}}^{n+1} + \mathbf{N}_S^{n+1}\ddot{\mathbf{Q}}^{n+1} = \mathbf{B}^{n+1} \\
&\mathbf{F}_F^{n+1} = \mathbf{F}_{vol}^{F^{n+1}} - \mathbf{F}_{transport}^{n+1} - \mathbf{F}_{pressure}^{n+1} \\
&\mathbf{F}_S^{n+1} = \mathbf{F}_{vol}^{S^{n+1}} - \mathbf{F}_{internal}^{n+1}
\end{aligned}
\tag{6}
$$

The mass matrices $\mathbf{M}_S$ and $\mathbf{M}_F^{n+1}$, for structures and fluids respectively, are made diagonal by classical mass lumping techniques (see for instance Argyris and Mjelnek, 1991). The matrix $\mathbf{M}_F^{n+1}$ is variable with time for fluids due to the Eulerian/ALE representation. The internal forces $\mathbf{F}_{internal}$ result from the integration of the elementary stresses for the structure, whereas the forces $\mathbf{F}_{pressure}$ result from the integration of the elementary pressure only for the fluid. $\mathbf{F}_{transport}$ are the nodal explicit transport forces for the fluid, resulting from the integration of the convective term in a Finite Element framework.

One major and original feature of the proposed solver built over the years is the dual management of kinematic constraints. The matrices $\mathbf{N}_F^{n+1}$ and $\mathbf{N}_S^{n+1}$ account for links expressing boundary conditions, fluid-structure interaction links and structural links, such as unilateral contact. The corresponding forces appear in the equilibrium equation as the Lagrange Multiplier vector $\mathbf{\Lambda}^{n+1}$ (see Faucher, 2014 for details). These kinematic constraints are in general non-permanent (i.e. links can appear and disappear at each time step) and even for persistent links, the coefficients in the coupling matrices need to be updated due to the changes in the geometric configuration of the linked entities. Building and updating the link operators is thus a significant computational task within one step of the explicit integration. It especially involves spatial sorting procedures to select the entities to be connected by contact conditions or fluid-structure interaction links. These sorting computations are of specific interest for the design of the relevant mesh refinement indicators introduced further in this paper and one implementation of immersed boundary-type fluid-structure links is given in Figure 1 (from basic principles found in Casadei, 2008).

One last characteristic of great importance of the numerical system described above is that is does not introduce any arbitrary parameter with direct effect on the physical solution (such as penalty coefficients for instance). The modeling effort is thus dedicated to geometry and meshing on the one hand, and to choosing and identifying the suitable constitutive laws and equations of state for all components of the system on the other hand.

The extension of the framework that will be introduced in Section 3 to handle multi-purpose mesh adaptivity obviously comes with some specific new parameters orienting the adaptation process. To preserve the benefits of the existing approach, their influence will be studied in depth in Section 4 to provide robust *a priori* values for the industrial simulations of Section 5, and to avoid any *a posteriori* calibration prior to confronting the results to experimental data.

3. Multi-purpose mesh adaptivity with new easy-to-compute and easy-to-combine refinement indicators

One major contribution of the current article is to start from the early implementation of an appropriate mesh refinement strategy for some features introduced in Section 2 separately (see Casadei et al. 2013 or Verdugo et al., 2014) and to extend it widely to be able to freely and efficiently combine refinement indicators for fluid and structure simultaneously, yielding a multi-purpose framework applicable to fully coupled cases of industrial complexity (including a proper parallel solver).

3.1 Short bibliography and description of the previously selected mesh refinement strategy

Among the numerous techniques available for mesh adaptivity (see Figure 2 for a quick classification in the illustrative situation of a singularity located in one corner of a rectangular domain, and refer to Barbier et al., 2014 for a more general review of adaptive methods), we focus for the present paper on *h-refinement* for unstructured meshes with *hanging* nodes allowed, i.e. nodes generated on edges or faces of neighbor cells with a different refinement level (see Figure 2-a).

This choice is motivated by the following arguments.

An approach based on *p-refinement* would require specific developments for Finite Elements with high-order shape functions and Finite Volumes with enhanced reconstruction algorithms benefiting from the added evaluation points; such developments are not straightforward for the generic computational framework introduced above and would require a dedicated research work.

Implementing *s-refinement* could be handled through the ALE formalism available in the proposed framework, with the development of suitable mesh-motion algorithms designed to balance the cell sizes to satisfy a specific error indicator; the potential of this approach is nevertheless limited due to its general lack of robustness regarding the mesh motion and to the fixed number of nodes.

Finally, among possible approaches based on *h-refinement* and compatible with non-cartesian geometries, the choice of an explicit time-integration scheme excludes multi-grid approaches designed to speed-up the convergence of implicit solvers, and patch-based methods compatible with explicit solvers come with specific algorithms for kinematic continuity and convective fluxes between overlapping meshes, which would require additional research to handle accurately and simultaneously fluid-structure interaction and liquid-gas interfaces. Moreover, solutions with no hanging node (i. e. node generated on an edge or a face of neighbor cells with a different refinement levels) bring constraints on the type of cells to be used (since only resorting to triangles in 2D and tetrahedra in 3D allows the elimination of hanging nodes in the mesh refinement process for unstructured grids), whereas the choice of a suitable discretization method is preferred to be related only to the proper modeling of the considered physics.

Before going further with the actual description of the selected strategy, it can be noticed that anisotropic mesh adaptation is notably not considered in the present paper, although producing very interesting results for multi-component flows (Coupez et al., 2013) or crack detection and tracking (Artina et al., 2015). Despite its promising qualities, it again introduces limitations regarding the proposed general physical and numerical framework, in

addition to be classically restricted to triangles and tetrahedra: features must be added to the solver (for fluid or structure) to correctly handle the high stretching levels of the adapted cells, which are very specific to some types of flow or some damage representations (for instance incompressible flow or phase field damage modeling respectively).

The basic mesh adaptation scheme, designed in Casadei et al., 2013, is described in Figure 3. The resulting hanging nodes need additional kinematic relations, which are managed as non-permanent constraints in the coupled system introduced above with no modification. This strategy benefits directly from the robust efficient management of such links introduced in Paragraph 2.2.

The adaptation of convective fluxes through the faces between cells at different refinement levels is also straightforward for first order Finite-Volume schemes used in the present paper. Preserving higher order approximations in the mesh transition zones would require an adaptation of the reconstruction procedures on faces between neighbor cells, for which many results are available in the literature (see for instance Castro et al., 2014).

Potential edge hanging nodes are identified in red in Figure 3, with the corresponding kinematic relations linking the hanging node variables to the variables attached to the nodes at the tips of the edge:

$$\left[\dot{\mathbf{Q}}\right]_k = \frac{1}{2}\left(\left[\dot{\mathbf{Q}}\right]_i + \left[\dot{\mathbf{Q}}\right]_j\right) \textit{(structure)} \text{ or } \left[\mathbf{U}\right]_k = \frac{1}{2}\left(\left[\mathbf{U}\right]_i + \left[\mathbf{U}\right]_j\right) \textit{(fluid)} \tag{8}$$

Face hanging nodes can occur only with hexahedra and are identified in green in Figure 3, with the corresponding kinematic relations linking this time the hanging node variables to those of the cell vertices:

$$\left[\dot{\mathbf{Q}}\right]_n = \frac{1}{4}\left(\left[\dot{\mathbf{Q}}\right]_i + \left[\dot{\mathbf{Q}}\right]_j + \left[\dot{\mathbf{Q}}\right]_l + \left[\dot{\mathbf{Q}}\right]_m\right) \textit{(structure)} \text{ or } \left[\mathbf{U}\right]_n = \frac{1}{4}\left(\left[\mathbf{U}\right]_i + \left[\mathbf{U}\right]_j + \left[\mathbf{U}\right]_l + \left[\mathbf{U}\right]_m\right) \textit{(fluid)} \tag{9}$$

Another advantage of the chosen strategy is its simplicity and robustness for field updates during splitting and unsplitting of cells (see Table 2). All the updates are exact, except for elementary internal variables during unsplitting (see Equation (10-c)). It is noticeable that in our case this latter situation occurs only for total stress and history internal variables in structures and that unsplitting is classically forbidden through the suitable indicator in zones with a significant gradient of internal variables. More precisely, unsplitting is currently activated when adaptivity is used to track elastic wave fronts (or pressure waves in fluids), but it becomes unlikely where non-linear mechanisms have been triggered in the material.

For a multi-component fluid model during unsplitting, Equations (10-a) and (10-b) must also be applied to each component, to compute the per-component densities, energies and volumes, from which the volume and mass fractions for the unsplit cell are directly obtained.

3.2 New class of easy-to-combine refinement indicators

A series of indicators is proposed in this section, with the primary objective of being potentially combined with no restriction. They are classified into two main categories. Local indicators are computed from local values of elementary fields (such as pressure gradients or threshold of one specific internal variable) or nodal fields (such a

displacement or velocity curvature), whereas proximity indicators are computed from the distance to a physical entity in the model (for instance to refine the fluid close to the structure or close to a physical interface).

While local indicators are directly taken from previous work, mainly from Casadei et al. 2013 and Verdugo et al., 2014, the new formulation for proximity indicators is one key innovative step of the present article.

3.2.1 Local indicators

The first category is composed of local gradient-based, curvature-based and threshold based indicators. For the first two, an associated error indicator e can be computed through:

$$|e| = Ch\|\mathbf{G}\| \ (\textit{gradient}) \text{ or } |e| = Ch^2 \max\left(|k_1|,|k_2|\right) \ (\textit{curvature}) \tag{11}$$

where C is a user-defined constant,

h is the current cell size,

$\mathbf{G}$ is the gradient of the chosen variable,

k_1 and k_2 are the principal curvatures of the chosen variable.

The objective size $\tilde{h}_i$ for each cell i subject to adaptivity with the current indicator, defining its objective refinement level l, is obtained from a user-prescribed error $\tilde{e}$ through the formula:

$$\tilde{h}_i = \sqrt{\frac{\tilde{e}}{e_i} h_i} \ ; \ l = \text{int}\left(\frac{h_i}{\tilde{h}_i}\right) \tag{12}$$

To avoid an uncontrolled increase of the number of cells for low user-prescribed error, the refinement level field computed above is often practically limited by an additional user-defined maximum level. In such a case, the indicator is still fully efficient for locating the zones where the mesh must be refined, but the prescribed error is not always reached.

For local threshold-based indicators, the refinement level is set to vary from 1 to a user-defined maximum level n when the monitored internal variable W within one concerned cell varies from a minimum value W_{min} triggering the mesh adaptation to a maximum value W_{max} above which the refinement level is kept constant:

$$l = \text{int}\left[1 + \frac{n\left(W - W_{min}\right)}{W_{max} - W_{min}}\right] \tag{13}$$

3.2.2 Proximity based-indicators

These indicators are of primary importance when dealing with fluid-structure interaction or physical interfaces, where an increased accuracy is mandatory to capture preponderant phenomena in the close vicinity on the involved entities. Some tentative formulations have been proposed (see again for instance Casadei et al. 2013), but they are mostly specific to one kind of interface problem and therefore lack the mandatory versatility to be

efficiently combined into models of industrial complexity. A new unified framework is therefore designed, consisting in two steps:

1. build at each time step a point cloud representing the shape of the reference entity (see Figure 4 and Figure 5 for the way to derive the point cloud from the various entities introduced above),
2. for each cell to be refined according to the indicator, find the point of the cloud closest to the cell centroid (which is topologically very similar to finding the projection of the centroid onto the reference entity) and set the refinement level from the distance r between the two points using the expression:

$$l = \mathrm{int}\left[\frac{(n+1)R - \min(r, nR)}{R}\right] \tag{14}$$

where R is an influence radius associated by the user to the reference entity,

n is the maximum refinement level associated to the current indicator, again set by the user.

One key advantage of the point cloud strategy is its computational efficiency, since the spatial search of the reference point in the cloud for the centroid of a given cell is a classical operation already implemented and optimized for the building of kinematic links (for instance for immersed boundary-type fluid-structure links, see Section 2.2 and Figure 1).

When building a point cloud for mesh refinement close to a structure, the density of the cloud is adjusted to the user-defined radius. The primary cloud points (in red in Figure 4) are placed at the centroids of the structural surface elements. They are used as such if the given radius exceeds the maximum distance between the element's vertices and its centroid. They are on the contrary replaced by auxiliary points placed at the centroids of subdivisions of the surface elements (in green in Figure 4) for smaller radii, with the subdivision level adjusted so that the distance between one point and its closest neighbor in the cloud never exceeds the radius.

For point clouds built to set the mesh refinement close to an interface, it is noticeable that the point distribution is almost independent from the parameter C as long as the jump of the field of interest remains sharp (i. e. the mixture zone is located in a one-cell thick layer, see Figure 5). This is achieved for the liquid-gas model introduced in Section 2.1 by preventing the numerical dissipation of the gas volume fraction through the VOFIRE scheme (see Section 2.2 for references).

Finally, the combination of all the proposed indicators is straightforward, by simply taking for one cell the maximum of all indicated refinement levels. A smoothing step is classically applied to the resultant refinement level field, to prevent jumps greater than 1 between one cell and its neighbors for a better accuracy.

3.3 Parallel implementation

Although not in the main scope of the current paper, full integration of the proposed adaptive strategy into an efficient parallel solver is mandatory for its application to the simulation of cases of industrial complexity. We focus on distributed memory issues, since a complementary shared memory parallel strategy (basically to speed up internal loops) can still be applied, with no modification due to mesh adaptivity. We thus refer to processing units

(abbreviated PU) as elementary units with their own memory and exchanging data through a network, one processing unit being possibly composed of several computing cores sharing its memory.

Some advanced work can be found on this topic in the literature (see for instance Berger and Oliger, 1984 ; Bergen et al., 2005 ; Sundar et al., 2007). In particular, methods based on forests of octrees appear to be close to the proposed framework and some significant steps regarding the scalability on hundreds of thousands of PUs have been taken with mesh management libraries like *p4est* (Burstedde et al., 2011). However, such applications act only on the mesh with the objective of strictly balancing the number of cells and faces among the available PU and limiting the data transfers between PU from one step to the next due to the mesh adaptation. This latter goal is achieved through a suitable numbering of cells based on a space filling curve (Mokbel and Aref, 2009), producing a list of cells which can be cut easily to attach a set of cells to each PU while preserving the connectedness of such groups and thus minimizing the size of the interfaces and the number of cell migrations from one PU to another during mesh adaptation.

Resorting to an external mesh management tool such a *p4est* for parallel computation is finally not relevant for our research, for the following reasons.

- Forests of octrees do not cover all the refinement situations defined in Figure 3. In particular, they are not compatible with triangular and tetrahedral base cells, which are especially needed for structural adaptation (see Sections 4 and 5).
- The load balancing is not related only to the number of cells attached to each PU when fluid-structure interaction occurs, particularly with immersed structures, since the necessary geometric operations to build the kinematic links and the computation of the corresponding reaction forces greatly contribute to the total computational cost of one time step and drastically increase when many linked structural and fluid nodes are attributed to different PUs,
- As a corollary to the latter point, the optimal domain decomposition for our kind of problems does not rely on mesh connectivity, but considers instead only the spatial proximity of the cells to attach them to a PU (see Faucher, 2014), to ensure the best locality of the kinematic links between fluid and structure (or between structures in contact) ; this contradicts the paradigm of the optimal mesh partitioning obtained from a space filling curve.

A specific parallel solver is thus derived from the existing domain decomposition formalism, applied to base cells only, and shall be described in details in future work, along with a particular load-balancing strategy based on periodic updating of the domain decomposition and a weighting procedure taking into account the different levels of refinement within each base cell, as well as the specific computational cost of each active cell (necessary to handle different kinds of elements and materials, for fluid and structure for instance, see again Faucher, 2014 for details on this topic). This is not implemented in the present research, so only low numbers of subdomains can be efficiently used and performance results are not provided. Anyway, to ensure that the introduced parallel strategy is

functional with no restriction regarding the general computational framework described in Sections 2.1 and 2.2, all the simulations presented in the paper are performed in parallel with 8 subdomains.

3.4 Verification test

This section provides a simple case implementing all the numerical features described above, for both physical modeling and mesh adaptivity, with the purpose at this point of verifying the algorithmic behavior of the proposed framework. The actual detailed evaluation of the methodology and its confrontation to experimental results are left for Sections 4 and 5. This test is inspired from an underwater explosion situation and especially exhibits an interaction between pressure waves followed through a gradient-based indicator and physical interfaces of different kinds, followed through proximity based indicators. The setup and the base mesh are given in Figure 6.

The results are displayed in Figure 7 in terms of pressure field in the fluid during 1 ms, when the pressure waves are the most significant in the system, and in Figure 8 in terms of water-air interface and structure motion up to 15 ms. Although the actual physical solution cannot be discussed for this particular test, the correct mesh refinement-unrefinement process along wave fronts is verified, as well as the expected capability of the adaptive solver to precisely capture and preserve sharp fluid interfaces. The absence of spurious pressure wave reflections through mesh transition is also verified in Figure 7 and is a direct consequence of the accurate management of constraints acting on hanging nodes through Lagrange Multipliers.

4. Parametric analysis of a simple 3D case implementing the interaction between a failing structure and a fluid with interface

Sections 4 and 5 are dedicated to the detailed evaluation of the capabilities of the proposed multi-purpose adaptive framework. The approach is driven by the comparison to the integral experiment described in Section 5. However, a first step is made using a simpler analytical model implementing similar physics (water pushed at high speed out of a tank through a failing plate, see Paragraph 5.1), to characterize the effect of various relevant physical and numerical parameters, such as the refinement processes in fluid and structure separately or the representation of the water-air interface.

4.1 Test setup and selected numerical models

The case consists of a liquid pushed through a plate with an initial crack. The geometry is simple so that several combinations of numerical methods and parameters can be tested, with the objective of drawing some relevant guidelines to be used when dealing with more complex physical systems, as in Section 5.

The physical characteristics of the case and the base meshes for fluid and structure, identical for all the performed simulations, are given in Figure 9.

We describe in Table 3 the 6 numerical models considered in the proposed parametric analysis. They are chosen to highlight separately the influence of the fluid modeling, in terms of both mesh adaptation and water-air interface management, and of the structural mesh refinement level. The material characteristics for air and water are those given in Figure 6, whereas the plate is made of AU4G 2024-T4 alloy used the final experiment and

described in Section 5. Structural elements where the failure occurs are deactivated (*element erosion*) and thus also removed from the fluid-structure interface, so that the fluid can flow through the opening cracks.

The base meshes are intentionally rather coarse to emphasize the benefits of adaptivity. The *edge refinement* introduced above corresponds to another kind of point cloud indicators with the points located in the centers of free structural edges, leading to refinement localized in the vicinity of the crack borders, improving the accuracy for the flow where it is mostly needed. Concerning adaptivity in structure, a threshold-base indicator is used (see Section 3.2 and Equation (13)) using the damage indicator from Equation (19), with 0 and 0.8 as minimum and maximum values respectively.

4.2 Results and interpretations

The simulation results are analyzed according to two complementary points of view (in accordance with the industrial context introduced in Section 1 and with the integral validation tests in Section 5):

- the prediction of the ultimate structural resistance, characterized by the final crack pattern,
- the prediction of initial conditions for secondary simulations involving the fluid projected across the structure, characterized by the shape of the water jet.

Depending on the numerical features they implement, models can answer positively to none, one or both of the objectives listed above, which has also to be cross-referenced with their computational cost to provide the expected guidelines for more complex tests, to be used in agreement with the actual applicative expectations associated with the simulations.

To present the physical solution of the problem introduced in Figure 9, the detailed results for Test 4 are given in Figure 10, for a simulated time of 25 ms, corresponding to the water jet impacting the opposite wall in the air domain.

For the comparisons between Test 1 to Test 4, we focus on the final crack pattern in the structure, obtained after 10 ms (Figure 11), and on the water-air interface representation after 20 ms (Figure 12), whereas for the comparisons between Test 4 to Test 6 in Figure 13,we follow the crack evolution in the plate from 3 ms to 10 ms.

For the presentation of the results in terms of crack propagation with respect to the maximum refinement level for the structure in below, Test 4 to Test 6 are reordered so as to place the various views in growing order of mesh refinement.

Figure 13 shows a dependence of both the crack pattern and the crack starting time from the refinement level (i. e. the cell size at the tip of the cracks). However, it is noteworthy that the crack velocity, once started, is approximately equal in all cases and that convergence is already achieved for the crack pattern in Test 4. It is also important to highlight that the observed mesh dependence is almost negligible between Test 4 and Test 6 after 10 ms, leading to the conclusion that the refinement level used in Test 4 is sufficient in the present case.

The general issue of mesh dependence for the crack starting time is well known (see for instance Geoffroy, 2010 or Song et al., 2008) and goes far beyond the scope of the current paper. In particular, it raises modeling questions in addition to purely computational ones. The continuous model indeed exhibits a strong singularity at both tips of the initial crack, producing a non-physical infinite stress state. Physically, the real stress state would be deduced from the initial thickness of the actual crack and should be recovered when the local cell size gets close to this value.

To complement on this topic, Figure 14-a provides the results obtained with a fully refined plate mesh with a cell size equal to that at the highest refinement level in Test 6. The crack starting time and the starting direction are again different from those in Test 4 and Test 6, and can approximately be retrieved by adding to Test 4 the initial forced refinement at the crack tips (see Figure 14-b and Figure 14-c), thus separating the effects of mesh refinement on crack initiation and crack propagation respectively. Anyway, given the statements above and in a technical field like structural failure in dynamics where solutions are classically not unique, especially when fluid-structure interaction is considered, these new solutions have no reason to be considered better than the solutions from Test 4 or Test 6 in Figure 13 and the suitable cell size at the tip of the cracks, as well as the parameters for mesh adaptation with respect to the local damage state, are thus to be specifically chosen taking into account some additional geometric elements, as well as experimental data if available.

We finally provide the computation times associated with all the tests run in this section in Table 4, on a strictly indicative basis due the non-optimum adaptive parallel solver currently penalized by high refinement levels increasing the load imbalance (see Section 2.3.4). It can be seen that the critical time step is classically imposed by the size of the structural elements, since the number of time cycles doubles when the maximum refinement level is increased by one. This confirms the conclusion from the above paragraph, since Test 6 is strongly penalized by the extra-refinement of the plate. The described situation can yet strongly evolve if a proper subcycling strategy is added to the proposed computational framework, which is rather classical with adaptivity and part of the prospects for our research (see in particular the work on spatial time-step partitioning for fast transient dynamics in Casadei and Halleux, 2009).

The second main lesson from Table 4 is that using the VOFIRE anti-dissipation scheme in the fluid approximately doubles the cost of the simulation, which is due to both the scheme itself and (more importantly) to the increase of the number of fluid cells induced by the associated refinement indicator.

5. High-resolution simulations of a complex integral experiment involving a failing tank under impact

5.1 Short presentation of the experimental program

An extensive description of the program can be found in Maurel, 2008 and Caleyron, 2012, also providing comparisons to simulation results obtained with *Smooth Particle Hydrodynamics* models (Monaghan, 1988), for both fluid and structure, also presented in Caleyron et al., 2013.

Using the drop tower from ONERA, Lille, France, it consists in a series of impacts on a steel tank filled with water and equipped at its bottom with an aluminum plate showing various openings to let the inner liquid leak. Figure 15 presents some views of the test bed and its principal dimensions.

Among the available tests, three are selected for their specific features summarized in Table 5 (reference names are taken from the original designation of the tests in the program). In all cases, the specimen is made of AU4G 2024-T4 aluminum alloy, whereas both the piston and the lateral tank surface are made of elastic steel. A sensor is implemented inside the tank, placed 3.75 cm above the bottom of the specimen, to measure the time evolution of the internal fluid pressure. The global validation process of the proposed computational methodology with confrontation against this test is as follows.

Firstly, Test E20A5 implements a simple and stiff specimen with a regular hole, so that the internal pressure in the tank is mostly influenced by the motion of the lateral tank surface and the internal pressure time history from this test is used to quantitatively evaluate the dynamic response of the mechanical model composed of the piston, the tank and the inner water.

Secondly, Test FXA5 additionally introduces a flexible specimen with large deflection and opening of a pre-cut strip with no structural failure. Again, internal pressure is directly influenced by the leaking flow rate and thus the structural motion, so that the related time history is used to quantitatively confront the capability of the proposed solver to accurately reproduce the interaction between the inner water and the specimen, given that the other fluid-structure interactions in the model have been validated from the previous test. The final shape of the specimen is also a direct consequence of the fluid-structure forces seen during the leaking transient, in terms of both global deflection of the plate and opening angle of the strip and this data thus yields another quantitative evaluation of the accuracy of the proposed computational methodology.

Finally, Test FXA5 adds damage and failure in the specimen, to complete the expected validation spectrum. The principal quantitative evaluation of the solving process comes from the final crack paths and lengths at the end of the simulation, directly influenced, as above, by the leaking transient and especially by the capability of the solver to reproduce the water flow through the opening cracks.

Secondary validation data are provided by high-speed camera views of the water jet in the visualization chamber below the test specimen. Relevant views are available for Tests E20A5 and FUA5 (see Figure 16). Due to the shape of the opening in the specimen in test FXA5, no distinct view of the jet is obtained with the camera. Moreover, as the water cast shadows on the specimen, no direct view of the structural strains and cracks is available either during the tests, so that quantitative comparison for structural behavior can only be made with the final shape of the specimen.

We emphasize the fact that if the primary features listed above provide solid, yet indirect, validation of the high accuracy of the multi-purpose adaptive framework built in the current paper, this secondary validation directly highlights the enhanced resolution coming from the proposed approach in terms of water-air interface tracking and liquid jet dynamics.

5.2 Numerical models

The common features of the models are described in Figure 17.

In all cases, for the sake of simplicity, the specimen is modeled with plate finite elements, even for Test E20A5, where it is rather thick. In this latter case, the size of the elements where the plate experiences the maximum bending is chosen relatively coarse to produce an acceptable ratio between planar dimensions and thickness.

For Test FXA5, two meshes are tested for the thin central part of the plate, in contact with water: one quadrilateral mesh and one triangular mesh, the latter inducing anisotropy which may prove useful for the crack propagation (even if the quadrangular mesh used in Section 4 does not suggest any need for extra anisotropy at this point). The different plate meshes are shown in Figure 18, where we identify in dark grey the part of the plate which is not in contact with the fluid. This part has the same thickness in all the tests (25 mm).

For all models, the material characteristics for air and water are again those given in Figure 6, both the piston and the lateral tank surface are made of elastic steel, whereas an elastic-thermoviscoplatic constitutive law with ductile failure is used for the specimen. The material law is shortly described in the next paragraph, as well as the identification of its parameters for the specific AU4G-2024-T4 alloy.

All the models implement the VOFIRE scheme for the representation of the water-air interface. It is deactivated (with no influence on the global solution) at the water-piston interface, since in this very configuration, where small amounts of water can pass through the interface due to the piston motion, preventing the dissipation inside the air domain can lead to numerical instabilities.

Parameters for mesh adaptivity used in the simulations are finally given in Table 6. It is chosen not to force any initial refinement at the crack tips for Test FXA5, taking into account that the actual initial notches are relatively thick (from the photographs of the specimen before testing, see Caleyron et al., 2013) and that an excessive stress concentration should thus be avoided in this configuration. Finally, due to the small size of the tank, mesh adaptation related to the pressure gradient is not implemented, since the waves travel fast in the water between the piston and the specimen, making the internal pressure rapidly almost homogeneous and the tracking of wave fronts unnecessary.

5.3 Material model for aluminum alloy AU4G 2024-T4 under impact leading to failure

5.3.1 Short description of the selected constitutive law

The material model is taken from the work from Aune et al., 2016, from the Norwegian University of Science and Technology, providing, in collaboration with the Joint Research Center of the European Commission, a model for elastic-thermoviscoplaticity and ductile failure particularly suited for steel and aluminum alloys under impact. It is based on the *modified* Johnson-Cook model (Johnson and Cook, 1983), where the strain-rate term is adjusted so as to avoid non-physical softening (Ortiz and Camacho, 1997, Børvik et al., 2001). The original representation of the strain hardening is also replaced by the saturation-type rule from Voce, 1948 to prevent numerical instabilities, so that the yield function writes:

$$f(\sigma) = \sigma_{eq} - \sigma_y = \sigma_{eq} - \left[A + Q_1\left(1 - e^{-C_1 p}\right) + Q_2\left(1 - e^{-C_2 p}\right)\right]\left(1 + \dot{p}^*\right)^C \left(1 - T^{*m}\right) \tag{15}$$

where σ_{eq} is the Von Mises equivalent stress,

A is the initial yield stress in the material,

p is the equivalent plastic strain, i. e. the energy-conjugated variable to the equivalent stress, while $\dot{p}$ is the equivalent plastic strain rate and $\dot{p}^* = \dot{p}/\dot{p}_0$ is the dimensionless plastic strain rate with $\dot{p}_0$ the reference strain rate,

T^* is the dimensionless temperature, expressed as $T^* = (T - T_r)/(T - T_m)$, with T the absolute temperature, T_r the absolute temperature of the room and T_m the absolute melting temperature,

Q_1, C_1, Q_2 and C_2 are material parameters used in the expression of the strain hardening term,

C is a material parameter used in the expression of the strain-rate hardening term,

m is a material parameter used in the expression of the temperature softening term.

Temperature is obtained from the thermal energy balance per unit volume using adiabatic conditions:

$$\chi \sigma_{eq} \dot{p} = \rho C_p \dot{T} \quad \Leftrightarrow \quad \dot{T} = \frac{\chi \sigma_{eq} \dot{p}}{\rho C_p} \tag{16}$$

where χ is the Taylor-Quinney coefficient representing the fraction of the plastic power converted into heat (often set to 0.9 in the literature),

ρ is the density of the material,

C_p is its specific heat capacity.

The failure criterion associated to the model above is taken from Cockcroft and Latham, 1968, and is based on the plastic work per unit volume, expressed as:

$$D = \frac{W}{W_C} = \frac{1}{W_C} \int_0^p \langle \sigma_1 \rangle dp \tag{17}$$

where W_c is the failure material parameter, which can be found by integrating the major principal stress in a uniaxial tension test during the entire equivalent plastic strain path until the plastic strain at failure p_f.

$\langle \sigma_1 \rangle$ stands for the positive part of the first principal stress. Failure classically occurs when the damage parameter reaches 1. Though relatively simple, this criterion has given equally good results as more complex criteria and especially accounts for both deviatoric and hydrostatic stress states (see Børvik et al., 2009 ; Kane et al., 2011 ; Dey et al., 2006).

5.3.2 Quick identification of material parameters for aluminum alloy AU4G 2024-T4

We propose a quick identification based only on the quasi-static traction curve found in Suffis, 2004 and replicated in Figure 19. This strategy is supported by the following assumptions, which allow setting the parameters for the strain-rate hardening term and the temperature softening term (the density, elastic parameter and initial yield stress for plasticity are taken directly from Suffis, 2004):

- aluminum alloys are known to be rather insensitive to strain rate, so an arbitrary small value is chosen for the exponent parameter C, as well as a classical value for the reference strain rate $\dot{p}_0$ of very limited influence in the present case,
- the exact melting temperature for this specific alloy in the T4 state is hard to find, but a value of 620°C (893 K) is coherent with the range of values found in the literature for the AU4G 2024 series of alloys, and is therefore chosen,
- values from the literature are also chosen for the specific heat capacity and the Taylor-Quinney coefficient (see previous section),
- the exponent parameter m for the thermal softening term is simply set to 1.

Under these hypotheses, it is licit to identify the remaining parameters Q_1, C_1, Q_2 and C_2 of the strain hardening term from the quasi-static traction curve only, which is done through a basic Monte-Carlo analysis using a simple traction test on one single hexahedral finite element. Knowing the parameters above, the failure parameter W_c is easily adjusted to match the maximum strain at failure.

The results are given in Figure 19 in terms of reproduction of the reference strain-stress traction curve until failure and in Table 7 in terms of values for all the parameters to be used in Sections 4 and 5.

5.4 Simulation results and comparison with experimental data

5.3.1 Test E20A5

Figure 20 displays the water jet below the specimen throughout the simulation up to 1 ms, with an additional view of the mesh adaptation process in the fluid domain at time 1 ms. The time history of the internal tank pressure up to 1.5 ms, compared to experimental data, is presented in Figure 21.

The primary validation objective (i. e. the correct reproduction of the evolution of the pressure inside the tank can be considered as *achieved*. The general evolution of the pressure, the extremum levels and the signal main frequency are relatively correctly reproduced up to 0.5 ms. After that, the global pressure decay remains acceptable, but a significant phase shift appears, suggesting that the interaction between the tank vibration and the jet is not accurately captured. It must be taken into account that the low compressibility of the water makes this quantity rather sensitive to structural boundary conditions in the tank. A more accurate representation would require the gathering of additional technological data about the test mock-up.

We consider anyway that the obtained results validate the modeling of the lateral surface of the tank to be used in the next simulations especially dedicated to the analysis of the behavior of the bottom specimen.

The secondary validation objective related to the water shape is only *partially achieved*. The jet tips are very different in the experiment and in the simulation: the jet does not turn into a spray at its extremity and seems to travel faster in the simulation. Some oscillations are captured in the radius of the computed water jet, producing shapes quite close to the bulbs observed in Figure 19-a, but the simulation does not accurately reproduce the frequency of bulbs.

The difference between the computed and observed water jet tips result from two phenomena which are not accounted for in the proposed numerical model: phase change when the jet expands laterally just below the hole and fragmentation into droplets due to the friction against the air. Increasing the resolution of the jet representation in this situation logically emphasizes these modeling shortcomings, whose effects are much less significant with the more complex specimen openings in the next cases.

Concerning the radial oscillations in the jet, their presence demonstrates as above that some relevant characteristics of the coupled fluid-structure system are actually modeled, yet with a lack of accuracy regarding the matching frequencies between the tank and the jet. Again, going further is a specific research topic out of the scope of the current article, which focuses on the more realistic tests where the leaking jet is directly related to the dynamics of the specimen.

5.3.2 Test FUA5

We provide in Figure 22 the evolution of the water jet up to 1.8 ms.

Figure 23 then compares the simulated shape of the water jet after 1.25 ms to the experimental view from Figure 16-b and Figure 24 presents the time history of the internal tank pressure, again compared to the experimental reference.

We provide in Figure 25 views of the final state of the plate. The simulation is not run until the elastic strain vanishes after the full draining of the tank, but the permanent plastic strain is fully established and does not evolve anymore after 1.5 ms.

The first primary validation objective related to the evolution of the pressure inside the tank is again considered as *achieved*. The general evolution of the pressure is correctly reproduced, and especially the global reduction of the pressure levels brought by the deformation of the specimen. The bad reproduction of the first peak questions the measures in this specific case, since this peak does not depend on the implemented specimen and the simulated level matches the one obtained in Test E20A5. This does not modify the given positive status.

The second primary objective is also *achieved*, since the final deflection of the specimen and opening angle of the strip are very accurately reproduced (see Figure 25-c). The slightly plastified zone on the contour of the plate sets the final curvature of the specimen whereas the significantly more plastified zones at the corners of the strip determine the angle between the strip and the rest of the plate, to be compared to the one on the photograph of the

specimen after the test. In both cases, the quantitative agreement between simulation and experiment is very satisfactory.

The secondary validation objective related to the shape of the water jet is also *achieved* with no restriction in this case. The angle of the jet is accurately captured, its length is correctly computed and the simulation especially reproduces the variation in the apparent jet curvature brought by the elastic springback of the metallic strip, validating indirectly the correct reproduction of the dynamics of the specimen. More qualitatively, this springback, occurring after 0.8 ms, results in the scattering of the primary water flow through the plate before the establishment of a secondary flow once the opening stabilized (with waves in the jet due to the residual oscillations of the strip).

5.3.3 Test FXA5

Figure 26 first displays some results obtained with the purely quadrangular mesh for the plate, in terms of water jet shape and structural failure pattern after 2 ms. The numerical solution does not show any significant defect, but it exhibits on the contrary an excessive isotropy in the plate failure process, helped by the very accurate and regular proposed computational framework. This configuration is thus discarded in favour of the second configuration with a triangular mesh in the failing part of the specimen, benefiting from the anisotropy brought by the triangles to get closer to the actual physics involved in the experiments.

The evolution of the water jet up to 2 ms in the selected configuration is then presented in Figure 27, whereas close-up views of the jet interacting with the cracks and of the mesh adaptation are provided in Figure 28.

Figure 29 then focuses on the crack pattern obtained with the triangular mesh for the specimen, with a comparison of both the shapes and lengths of the computed cracks to the experimental reference. It also presents the mesh adaptation process in the structure, allowing a very sharp representation of the cracks.

To illustrate the variations in the deflections of the petals due to fluid-structure interaction and secondary water flows, the vertical displacement at the tips of the petals are plotted in Figure 30, which also demonstrates that the simulation is stopped after the global elastic springback of the specimen and that the failing process is indeed actually terminated at time 2 ms.

Concerning the validation analysis for this particular test, it must be taken into account that introducing failure in the physical system inevitably yields some dispersion in the results (both experimental and numerical).

The primary validation objective can yet be considered as fully *achieved*. The final lengths of the cracks are very accurately reproduced in the simulation. The crack paths are in good agreement between simulation and experiment, especially in terms of average curvature. Like for the test FUA5, this is an indirect quantitative validation of the accuracy of the fluid-structure solver, obtained with no *a posteriori* calibration as stated in Section 2.

Concerning the secondary validation objective, related to the opening kinematics of the specimen, only qualitative statements can be given since the available photographs do not allow reliable displacement measures.

Anyway, by comparing the final shapes in Figure 29-b, we can affirm that the deflection amplitudes of the petals are correctly reproduced, as well as the variations between the deflections of the different petals (one opening significantly more the others).

The capture of secondary flows occurring horizontally at a very small scale between petals with different deflections was a major expectation for this test and represents a significant achievement of the proposed high-resolution computational framework, even though unfortunately no experimental result can directly confront these results.

6. Conclusion and prospects

A high-resolution computational framework combining accuracy and robustness through generic mesh adaptivity is proposed and fully described in the present paper, to provide advanced numerical results related to the response of fluid-structure systems under impact, with fluid interfaces and potential structural failures. The numerical characteristics of the coupled scheme are extensively analyzed through a parametric study based on a significant 3D test and it is then confronted against complex experiments with very satisfactory validation results.

Future steps will be driven by the need for a computational efficiency matching the physical capabilities of the introduced methodology, with two major well identified directions.

The first direction is related to time multi-scale algorithms, also called spatial time-step partitioning in some references, to overcome the problematics specific to explicit integration that the local reduction of the cell size with mesh adaptivity will classically result in a reduction of the global time step used for all the cells in the model. Making the time-step non-local through the proposed generalized subcycling techniques, which allows to account also for the evolution of the stability condition with the grid motion, is a solution frequently discussed in the literature, and it still has to be made fully compatible with scalable parallel algorithms, since it often goes against the optimization of the load balancing among numerous computational units.

The second direction is especially dedicated to high-performance computing (with an optimized time-stepping approach or not), with the requirement of implementing into the parallel framework the same level of adaptivity as it is done for the mesh. It has been shown that the complex physics addressed in the proposed research, and particularly fluid-structure interaction, reaches the limits of strongly optimized mesh adaptation libraries due to the need for partitioning techniques unrelated to the mesh connectivity, which breaks the paradigm for their high-level scalability and forces the development of new and rather specific adaptive parallel algorithms.

References

1. Argyris, J., Mlejnek, H.-P., 1991. Dynamics of structures. Texts on Computational Mechanics, Volume V, North Holland.
2. Artina M., Fornasier M., Micheletti S., Perotto S., 2015. Anisotropic Mesh Adaptation for Crack Detection In Brittle Materials. SIAM Journal on Scientific Computing, 37(4), 633-659.
3. Aune V., Valsamos G., Casadei F., Larcher M., Langseth M., Børvik T., 2016. Numerical study on the structural response of blast-loaded thin aluminium and steel plates. International Journal of Impact Engineering 99, 131-144.
4. Barbier L., Ramière I., Lebon F., 2014. Strategies involving the local defect correction multi-level refinement method for solving three-dimensional linear elastic problems. Computers and Structures 130, 73-90.
5. Barras G., Souli M., Aquelet N., Couty N., 2012. Numerical simulation of underwater explosions using an ALE method. The pulsating bubble phenomena. Ocean Engineering 41, 52-66.

6. Bergen B.K., Hülsemann F., Rüde U., 2005. Is 1.7×1010 unknowns the largest finite element system that can be solved today? In SC '05: Proceedings of the ACM/IEEE International Conference for High Performance Computing, Networking, Storage, and Analysis, ACM, New York.
7. Berger M.J. and Oliger J., 1984. Adaptive mesh refinement for hyperbolic partial differential equations. Journal of Computational Physics 53, 484-512.
8. Børvik T., Hopperstad O. S., Berstad T., Langseth M., 2001. A computational model of viscoplasticity and ductile damage for impact and penetration. European Journal of Mechanics - A/Solids 20, 685-712.
9. Børvik T., Dey S., Clausen A.H., 2009. Perforation resistance of five different high-strength plates subjected to small-arms projectiles. International Journal of Impact Engineering 36, 948-964.
10. Brar G. S., Singh S., 2014. An Experimental and CFD Analysis of Sloshing in a Tanker. 2nd International Conference on Innovations in Automation and Mechatronics Engineering, Procedia Technology 14, 490-496.
11. Burstedde C., Wilcox, L.C., Ghattas, O., 2011. p4est: scalable algorithms for parallel adaptive mesh refinement on forest of octress. SIAM Journal of Scientific Computing 33(3), 1103-1133.
12. Caleyron F., 2012. Simulation numérique par la méthode SPH de fuites de fluide consécutives à la déchirure d'un réservoir sous impact. PhD thesis, Institut National des Sciences Appliquées, Lyon, France.
13. Caleyron F., Combescure A., Faucher V., Potapov S., 2013. SPH modeling of fluid–solid interaction for dynamic failure analysis of fluid-filled thin shells. Journal of Fluids and Structures 39, 126-153.
14. Casadei, F., 2008. Fast transient fluid–structure interaction with failure and fragmentation. In: 8th World Congress on Computational Mechanics, June 30–July 5, Venice, Italy.
15. Casadei, F., Díez, P., Verdugo, F., 2013. An algorithm for mesh refinement and un-refinement in fast transient dynamics, International Journal of Computational Methods 10, 1-31.
16. Casadei and Halleux, 2009. Binary spatial partitioning of the central-difference time integration scheme for explicit fast transient dynamics, International Journal for Numerical Methods in Engineering, 78, 1436-1473.
17. Castro D.A., Gomes S.M., Jorge Stolfi J., 2014. High-order adaptive finite-volume schemes in the context of multiresolution analysis for dyadic grids. Computational and Applied Mathematics 35(1), 1-16.
18. Chiapolino A., Boivin P., Saurel R., 2017. A simple and fast phase transition relaxation solver for compressible multicomponent two-phase flows. Computers and Fluids 150, 31-45.
19. Cockcroft M.G., Latham D.J., 1968. Ductility and the workability of metals. Journal of the institute of metals 96, 33-39.
20. Coupez T., Jannoun G., Nassif N., Nguyen H.C., Digonnet H., Hachem E., 2013. Adaptive time-step with anisotropic meshing for incompressible flows. Journal of Computational Physics 241, 195-211.
21. Deletombe E., Fabis J., Dupas J., Mortier J. M., 2013. Experimental analysis of 7.62 mm hydrodynamic ram in containers. Journal of Fluids and Structures 37, 1-21.
22. Després, B., Lagoutière, F., Labourasse, E., Marmajou, I., 2010. An anti-dissipative transport scheme on unstructured meshes for multicomponent flows. International Journal on Finite Volumes 7, 30-65.
23. Dey S., Børvik T., Hopperstad O.S., Langseth M., 2006. On the infuence of fracture criterion in projectile impact of steel plates. Computational Materials Science 38, 176-191.
24. Donea, J., Huerta, A., Ponthot, J.Ph., Rodriguez-Ferran, A., 2004. Arbitrary Lagrangian–Eulerian Methods. In Encyclopedia of Computational Mechanics, Edited by Erwin Stein, René de Borst and Thomas J.R. Hughes. Volume 1: Fundamentals.
25. Faucher, V., Kokh, S., 2013. Extended Vofire algorithm for fast transient fluid-structure dynamics with liquid-gas flows and interfaces. Journal of Fluids and Structures 39, 102-125.
26. Faucher, V., 2014. Advanced parallel strategy for strongly coupled fast transient fluid-structure dynamics with dual management of kinematic constraints. Advances in Engineering Software 67, 79-89.
27. Faucher V., Bulik M., Galon P., 2017. Updated VOFIRE algorithm for fast fluid–structure transient dynamics with multi-component stiffened gas flows implementing anti-dissipation on unstructured grids. Journal of Fluids and Structures 74, 64-89.
28. Geffroy A.-G., 2010. Modélisation numérique de la rupture de structures navales sous l'effet d'explosions au contact. PhD thesis, Université de Bretagne Sud, France.
29. Harlow, F., Amsden, A., 1971. Fluid Dynamics. Monographe LA-4700, Los Alamos National, Laboratory, NM.
30. Jeon S.-J., Jin B.-M., Kim Y.-J., 2012. Assessment of the fire resistance of a nuclear power plant subjected to a large commercial aircraft crash. Nuclear Engineering and Design 247, 11-22.
31. Johnson G.R., Cook W.H., 1983. A Constitutive Model and Data for Metals Subjected to Large Strains, High Strain Rates and High Temperatures. In: Proceedings of the 7th International Symposium on Ballistics, The Hague, 541-547.
32. Kane A., Børvik T., Benallal A., Hopperstad O.S., 2011. Failure criteria with unilateral conditions for simulation of plate perforation. European Journal of Mechanics - A/Solids 30, 468-476.
33. Le Métayer, O., Massoni, J., Saurel, R., 2003. Elaborating equation of state of a liquid and its vapor for two phase flow models. International Journal on Thermal Sciences 43, 265-276.
34. Lin F., Tang H., 2017. Nuclear containment structure subjected to commercial aircraft crash and subsequent vibrations and fire. Nuclear Engineering and Design 322, 68-80.
35. Maurel B. , 2008. Modélisation par la méthode SPH de l'impact d'un réservoir rempli de fluide. PhD thesis, Institut National des Sciences Appliquées, Lyon, France.
36. Mokbel M.F., Aref W.G., 2009. Space-Filling Curves. In: Liu L., Özsu M.T. (eds) Encyclopedia of Database Systems. Springer, Boston, MA.
37. Monaghan J.J., 1988. An introduction to SPH. Computer Physics Communications 48, 88-96.
38. Nicolici S., Bilegan R. M., 2013. Fluid structure interaction modeling of liquid sloshing phenomena in flexible tanks. Nuclear Engineering and Design 258, 51-56.
39. Ortiz M., Camacho G.T., 1997. Adaptive Lagrangian modelling of ballistic penetration metallic targets. Computer Methods in Applied Mechanics and Engineering 142, 269-301.
40. Panciroli R., Ubertini S., Minak G., Jannelli E., 2015. Experiments on the dynamics of flexible cylindrical shells impacting on a water. Experimental Mechanics 55, 1537-1550.
41. Schiffer A., Tagarielli V. L., 2015. The response of circular composite plates to underwater blast: Experiments and modelling. Journal of Fluids and Structures 52, 130-144.
42. Song J.-H., Wang H., T. Belytschko T., 2008. A comparative study on finite element methods for dynamic fracture. Computational Mechanics, 42(2), 239-250.

43. Suffis A., 2004. Développement d'un modèle d'endommagement à taux de croissance contrôlé pour la simulation robuste de ruptures sous impact. PhD thesis, Institut National des Sciences Appliquées, Lyon, France.
44. Sundar H., Sampath R.S., Adavani S.S., Davatzikos C., G. Biros G., 2007. Low-constant parallel algorithms for finite element simulations using linear octrees. In SC '07: Proceedings of the ACM/IEEE International Conference for High Performance Computing, Networking, Storage, and Analysis, ACM, New York.
45. Van Nuffel D., Vepa K.S., De Baere I., Degrieck J., De Rouck J., Van Paepegem W., 2013. Study on the Parameters Influencing the Accuracy and Reproducibility of Dynamic Pressure Measurements at the Surface of a Rigid Body During Water Impact. Experimental Mechanics 53(2), 131-144.
46. Verdugo, F., Parés, N., Díez, P., 2014. Error assessment in structural transient dynamics. Archives of Computational Methods in Engineering, 21-59.
47. Voce E., 1948. The relationship between stress and strain for homogenous deformation. Journal of the Institute of Metals 74, 536-562.

Tables

c	sound speed	P^{∞}	parameter for stiffened gases accounting for the molecular attraction effects
c_i	mass fraction for component *i*	$\mathbf{N}_F^{n+1}$	fluid connection matrix at step *n*
α_i	volumetric fraction for component *i*	$\mathbf{N}_S^{n+1}$	structural connection matrix at step n
$\mathbf{f}_{S\to F}$	structural forces on fluid	P	fluid pressure
$\mathbf{f}_{F\to S}$	fluid forces on structure	E	fluid total energy
$\mathbf{F}_{vol}^{F^{n+1}}$	nodal fluid body forces at step *n+1*	$\mathbf{q}$	structural displacement
$\mathbf{F}_{vol}^{S^{n+1}}$	nodal structural body forces at step *n+1*	$\mathbf{Q}^{n+1}$	nodal structural displacement at step *n+1*
$\mathbf{F}_{transport}^{n+1}$	nodal fluid transport forces at step *n+1*	$\mathbf{u}$	fluid velocity
$\mathbf{F}_{internal}^{n+1}$	nodal structural internal forces at step *n+1*	$\mathbf{U}^{n+1}$	nodal fluid velocities at step *n+1*
$\mathbf{F}_{pressure}^{n+1}$	nodal fluid pressure forces at step *n+1*	$\boldsymbol{\varepsilon}$	structural strain tensor
$\mathbf{M}_F^{n+1}$	variable mass matrix for fluid at step *n+1*	$\boldsymbol{\sigma}$	structural stress tensor
$\mathbf{M}_S$	constant mass matrix for structure	$\boldsymbol{\Lambda}^{n+1}$	Lagrange multipliers at step *n+1*
γ	specific heat ratio for gases and stiffened gases	ρ	fluid density
q	formation energy for stiffened gases		

Table 1 : Nomenclature for Section 2

Field update when splitting a cell	Field update when unsplitting a cell
Nodal displacement and velocity for new nodes: obtained from field reconstruction through shape functions inside master element (acceleration computed during the next explicit time step) *Element variables within split cells*: - density, fluid total energy, total stress and internal variables copied from master element, - no need to transfer pressure (computed during the next explicit time step)	*Nothing to do for nodal variables* *Element variables within unsplit cell*: - compute density from total mass and volume: $\rho = \left(\sum_{\text{child } i} \rho_i V_i\right) / \left(\sum_{\text{child } i} V_i\right)$ (10-a) - compute fluid total energy (if needed) from total energy and mass: $E = \left(\sum_{\text{child } i} \rho_i E_i V_i\right) / \left(\sum_{\text{child } i} \rho_i V_i\right)$ (10-b) - compute total stress or internal variable $\mathbf{W}$ (a tensor in the general case) by taking the mean value from the children: $\mathbf{W} = \left(\sum_{\text{child } i} \mathbf{W}_i\right) / [\text{number of children}]$ (10-c) - no need to transfer pressure (computed during the next explicit time step)

Table 2: Field update during mesh adaptation

Basic model	*Progressive improvement of the fluid mesh adaptivity and modelling*		
Test 1 Adaptivity in structure and basic modeling for fluid	**Test 2** Adaptivity in structure and basic FSI adaption in fluid	**Test 3** Adaptivity in structure and additional edge refinement in fluid	**Test 4** Adaptivity in structure and VOFIRE scheme for fluid interface with associated refinement
Maximum refinement level in structure: 4 No refinement in fluid No anti-dissipation for water-air interface	Maximum refinement level in structure: 4 **Maximum refinement level for FSI adaption in fluid: 2** No anti-dissipation for water-air interface	Maximum refinement level in structure: 4 Maximum refinement level for FSI adaption in fluid: 2 **Maximum level for additional edge refinement in fluid: 3** No anti-dissipation for water-air interface	Maximum refinement level in structure: 4 **VOFIRE anti-dissipation for water-air interface** **Maximum refinement level for VOFIRE driven adaptivity: 3** Maximum level for additional edge refinement in fluid: 3

Sensitivity to the maximum structural refinement level	
Test 5 VOFIRE scheme in fluid and reduced adaptivity in structure	**Test 6** VOFIRE scheme in fluid and enhanced adaptivity in structure
Maximum refinement level in structure: 3 VOFIRE anti-dissipation for water-air interface Maximum refinement level for VOFIRE driven adaptivity: 3 Maximum level for additional edge refinement in fluid: 3	**Maximum refinement level in structure: 5** VOFIRE anti-dissipation for water-air interface Maximum refinement level for VOFIRE driven adaptivity: 3 Maximum level for additional edge refinement in fluid: 3

Table 3: Considered numerical models

	Test 1	**Test 2**	**Test 3**	**Test 4**	**Test 5**	**Test 6**
Number of time cycles	19 700	17 770	18 070	18 060	9 210	36 050
Elapsed time	1 085 s	3 129 s	1 7 131 s	36 170 s	16 330 s	71 614 s

Table 4: Indicative computation times for Test 1 to Test 6

Reference name	*Characteristics*	*Primary validation features*
E20A5	Thick specimen (thickness: 25 mm) Large circular hole (diameter: 20 mm) Impact velocity: 5 m.s^{-1}	Validation of the fluid-structure model in terms of water/tank/piston modeling. Validation data: internal tank pressure.
FUA5	Thin specimen (thickness: 2 mm) U-shaped initial crack (i.e. square strip with 3 free edges, edge length: 20 mm) Impact velocity: 5 m.s^{-1}	Additional validation of the fluid-structure interaction with strong coupling between flow and finite displacements of the specimen. Validation of the plasticity model. Validation data: internal tank pressure and final shape of the specimen (opening angle of the strip in particular).
FXA5	Thin specimen (thickness: 2 mm) X-shaped initial crack (i. e. 2 orthogonal notches of 20 mm each) Impact velocity: 5 m.s^{-1}	Additional validation of the failure model. Validation data: final crack paths in the specimen and opening kinematics.

Table 5: Selected tests for simulation/experiment comparison

Fluid-piston interface	**Fluid-specimen interface**	**Water-air interface**	**Structural damage and failure (test FXA5 only)**
Fluid-structure point cloud refinement indicator for the fluid Maximum level: **2**	Fluid-structure point cloud refinement indicator for the fluid Maximum level: **3**	VOFIRE point cloud refinement indicator for the fluid Maximum level: **3**	Threshold-based refinement indicator using damage variable from 0 to 0.8 Minimum level: **0** Maximum level: **4**

Table 6: Parameters for mesh adaptivity in fluid and structure

Density	*Elasticity*		*Strain hardening term for plasticity*				
ρ	E	ν	A	Q_1	C_1	Q_2	C_2
[kg.m^{-3}]	[Mpa]	[-]	[Mpa]	[Mpa]	[-]	[Mpa]	[-]
2 780	74 000	0.3	314	49.8	105	505	5

Strain-rate hardening term for plasticity		*Thermal softening term for plasticity*					*Failure*
C	$\dot{p}_0$	C_p	χ	T_r	T_m	m	W_c
[-]	[s^{-1}]	[J.Kg^{-1}.K^{-1}]	[-]	[K]	[K]	[-]	[MPa]
0.001	0.0005	910	0.9	293	893	1	156

Table 7: Final set of material parameters for AU4G 2024-T4

Figures

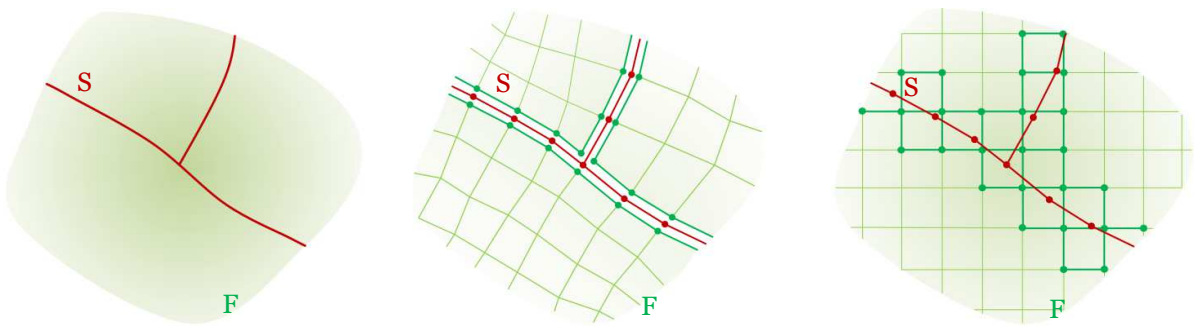

Continuous constraint:

$$\left(\dot{\mathbf{q}}_S - \mathbf{u}_F\right)\cdot\mathbf{n} = 0 \quad \text{(7-a)}$$

along the structure

Discrete constraint:

$$\left(\left[\dot{\mathbf{Q}}_S\right]_j - \left[\mathbf{U}_F\right]_i\right)\cdot\mathbf{n}_j = 0 \quad \text{(7-b)}$$

for each fluid node i on the fluid-structure interface, associated with the structure node j

Discrete constraint:

$$\left(\sum_{j=1}^{N}\left[\dot{\mathbf{Q}}_S\right]_j - \left[\mathbf{U}_F\right]_i\right)\cdot\tilde{\mathbf{n}}_S = 0 \quad \text{(7-c)}$$

for each fluid node i on the structure influence domain, associated with a set of N structural nodes defining an approximate normal direction $\tilde{\mathbf{n}}_S$

(a) Continuous system for shell structure (in red) immersed in a fluid

(b) Discrete model with conforming meshes for structure and fluid

Links are nodal and permanent (yet with variable coefficients due the evolution of the normal direction to the structure)

(c) Discrete model with immersed-boundary type links and independent meshes

Links are obtained at each time step by sorting the entities and associating each fluid node to the closest structural element or node

Figure 1: Two main classes of fluid-structure models and associated computational operations

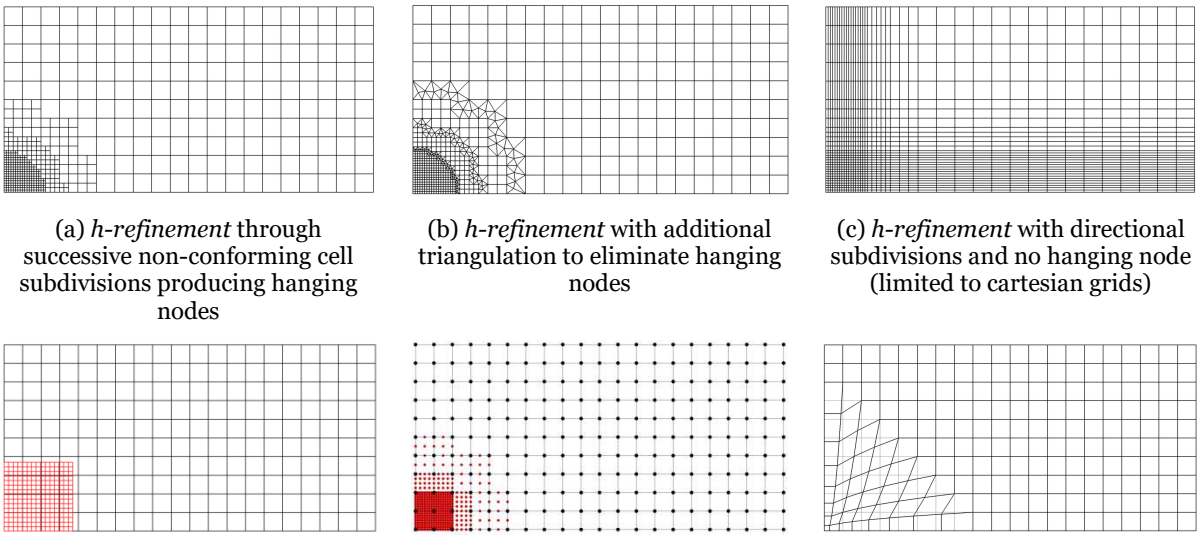

(a) *h-refinement* through successive non-conforming cell subdivisions producing hanging nodes

(b) *h-refinement* with additional triangulation to eliminate hanging nodes

(c) *h-refinement* with directional subdivisions and no hanging node (limited to cartesian grids)

(d) Patch-based *h-refinement*, close to multi-model and multi-grid techniques

(e) *p-refinement* through successive increases of the order of shape functions (producing new internal nodes, edge nodes and hanging nodes)

(f) *s-refinement* through dedicated grid motion keeping the number of nodes constant

Figure 2: Short classification of mesh adaptive refinement techniques

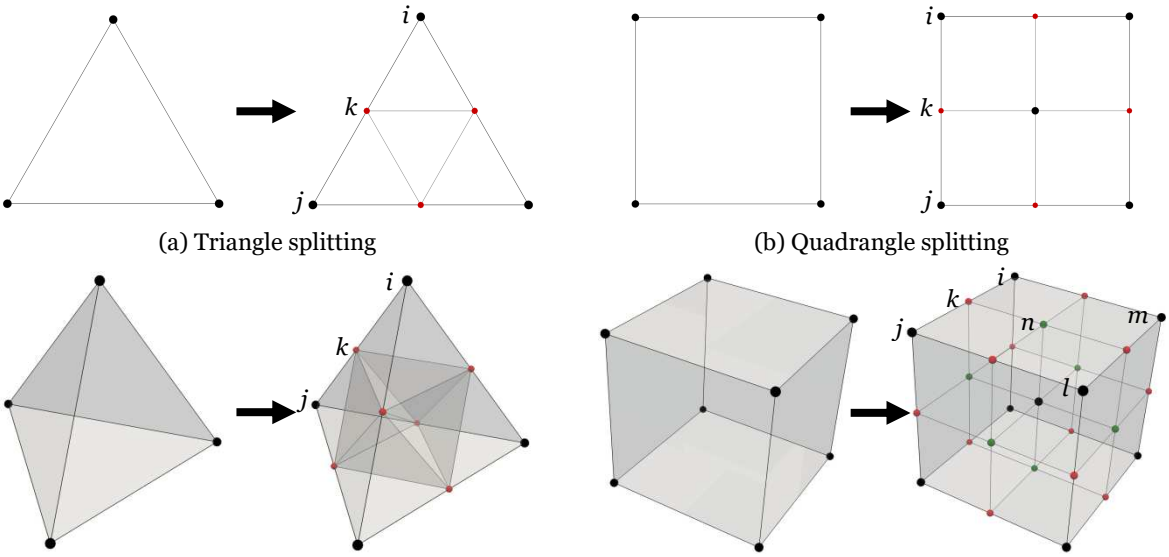

(a) Triangle splitting

(b) Quadrangle splitting

(c) Tetrahedron splitting

(d) Hexahedron splitting

Figure 3: Cell splitting scheme

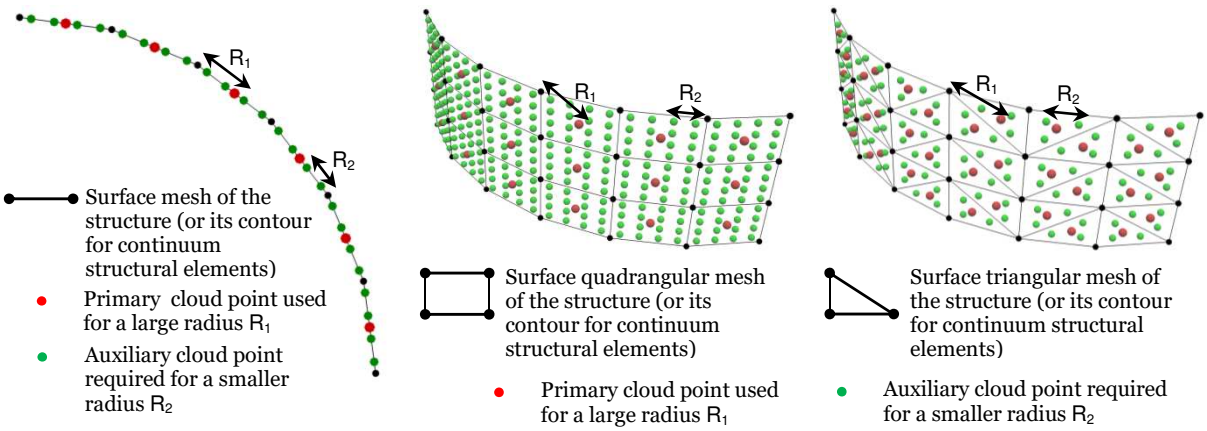

(a) 2D case

(b) 3D case

Figure 4: Point cloud building for fluid mesh refinement close to a structure

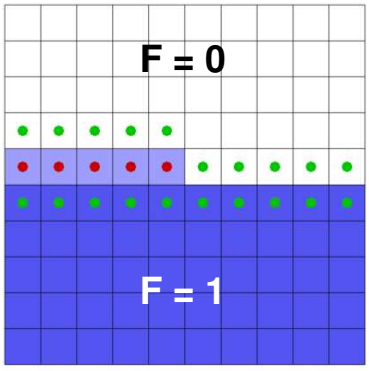

The interface is identified as the jump of an elementary field F, classically varying between 0 and 1 (for instance, the volume fraction of one component for a multi-component fluid model).

- Primary cloud points, placed at the centroids of cells where the value W of the field is such that:

$$C \le F \le 1 - C \tag{15-a}$$

where C is a user-defined strictly positive parameter.

- Secondary cloud points, placed at the centroids of cells for which the expression below, involving the cell's neighbors, holds:

$$\max_{i,j \in \text{neighbors}} \left(\left| F_i - F_j \right| \right) \ge C \tag{15-b}$$

Figure 5: Point cloud building for fluid mesh refinement close to an interface

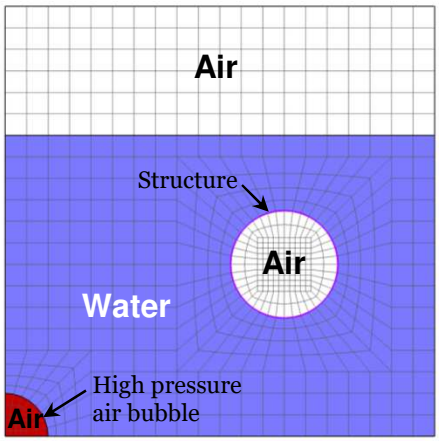

The structure is immersed in the water. Its mesh is initially aligned on the fluid mesh to accurately define the trapped air volume.

The contour of the fluid domain is a closed box.

Dimensions:

- Square box : 1 m x 1 m
- Air bubble initial radius: 0.1 m
- Structure initial radius: 0.2 m
- Structure thickness: 1 cm

Material parameters:

- Air (stiffened gas): P_{ini}=1 bar, ρ_{ini}=1 kg.m^{-3}, γ=1.4, P^{∞} = 0 bar, q = 0
- High pressure air bubble (stiffened gas): P_{ini}=100 bar, ρ_{ini}=100 kg.m^{-3}, γ=1.4, P^{∞} = 0 bar, q = 0
- Water (stiffened gas):): P_{ini}=1 bar, ρ_{ini}=1000 kg.m^{-3}, γ=4.4, P^{∞} = 4500 bar, q = 0
- Structure (elastic steel): ρ=7800 kg.m^{-3}, Poisson's ratio η=0.3, Young's modulus E=200.10^{9} Pa

Figure 6: Verification test - Setup and mesh

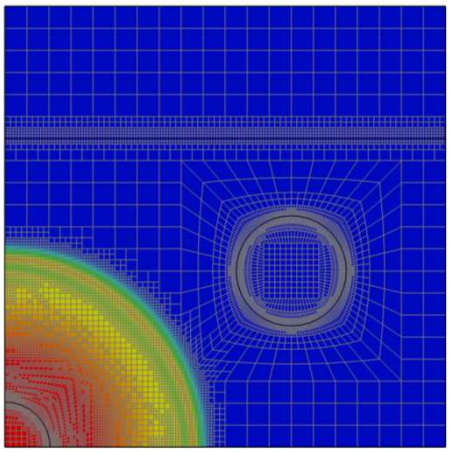

(a) Time = 0.25 ms

Primary wave propagation from the high pressure bubble

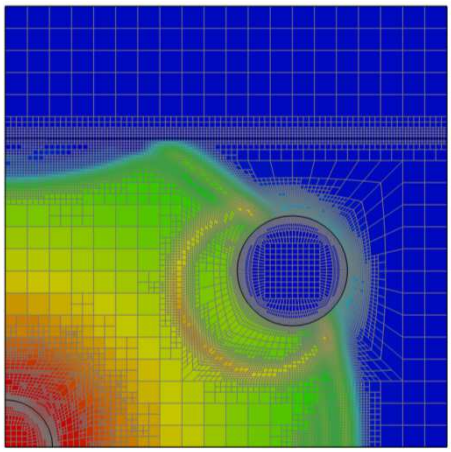

(b) Time = 0.5 ms

Primary wave reflection on both the structure and the water-air free interface (producing a rarefaction wave)

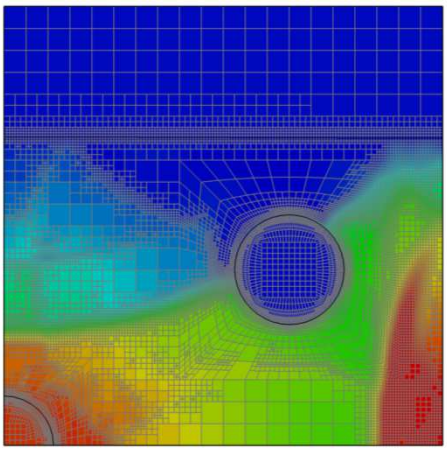

(c) Time = 0.75 ms

Interaction between reflected waves and primary wave reflection on the bottom right corner of the box

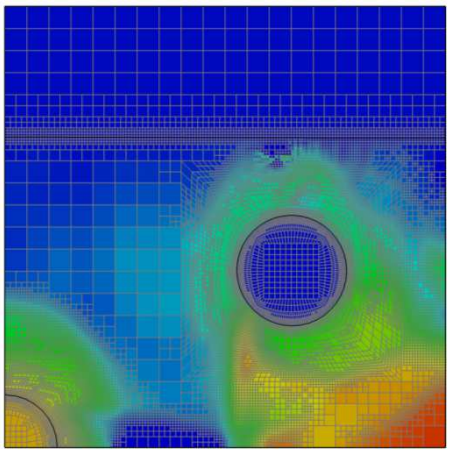

(d) Time = 1 ms

Multiple waves in the fluid domain and disappearance of a dominant wave pattern

Figure 7: Verification test - Pressure waves propagation in the fluid up to 1 ms

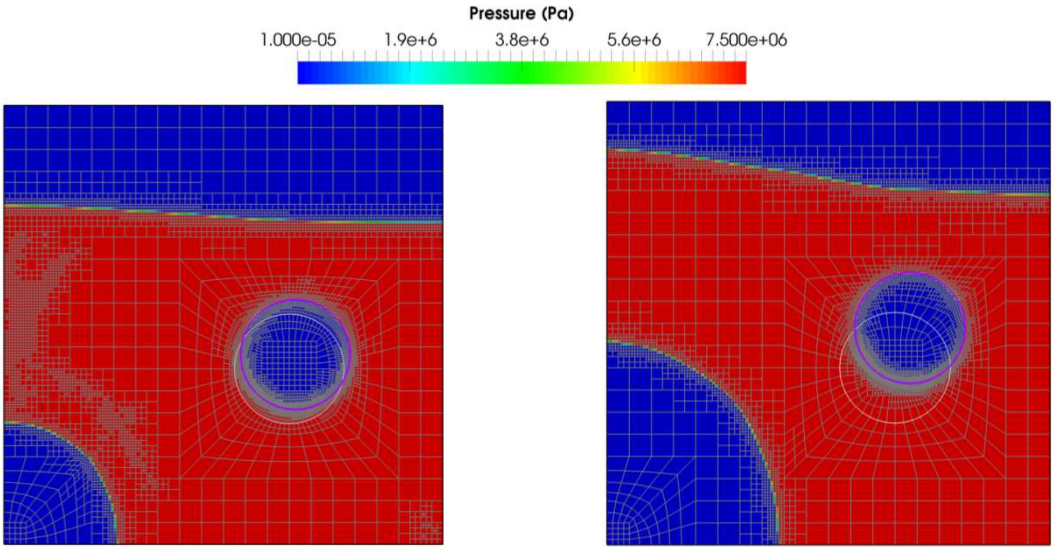

(a) Time = 5 ms

(b) Time = 10 ms

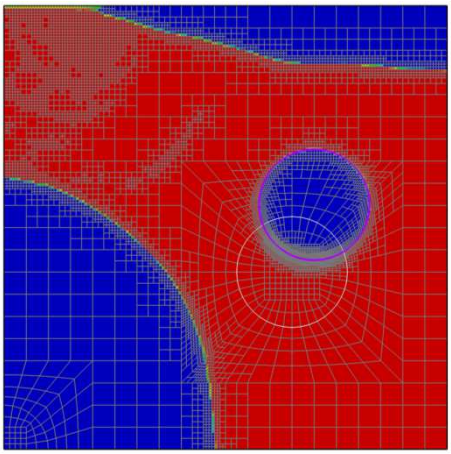

(c) Time = 15 ms

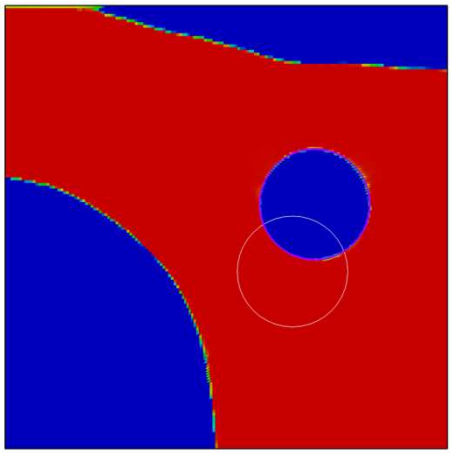

(d) Time = 15 ms, no mesh display for a better visualization of interfaces

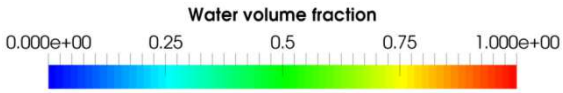

The initial location of the structure is displayed in white on the different views.

As expected, the refinement associated to the pressure gradient almost vanishes (it reappears when the water impacts the top left corner of the box).

The mesh refinement and the anti-dissipative VOFIRE scheme allow a sharp representation of the water-air interface. In particular, the trapped air volume inside the structure is perfectly conserved, as shown in (d).

Figure 8: Verification test – Structure and interface motion up to 15 ms

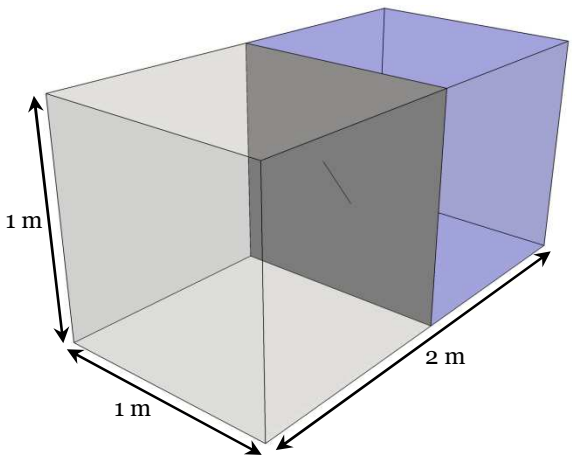

(a) General view

The envelope of the fluid domain is a rigid wall. The front compartment is filled with air and the back compartment (in blue) is filled with water. The structure presents a diagonal initial crack of length 21 cm.

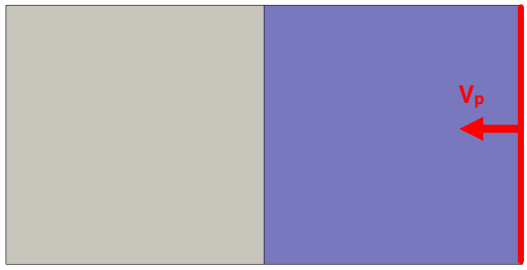

(b) Lateral view

The right face (in red) is moved to push the liquid through the plate (imposing an ALE representation for the fluid domain). The piston velocity Vp is set to 10 m.s^{-1} during 10 ms, and to zero thereafter. The fluid is initially at rest at the pressure of 1 bar.

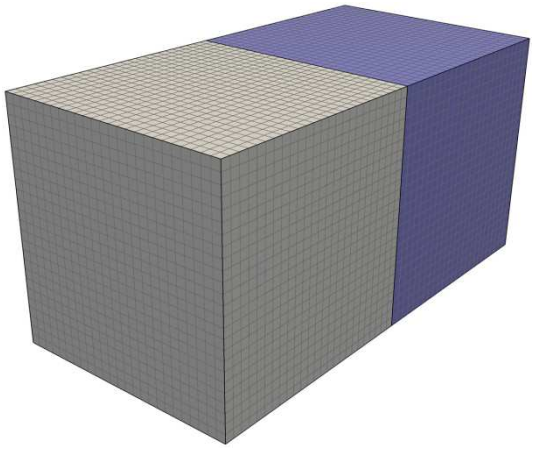

(c) Base fluid mesh (31 250 cells)

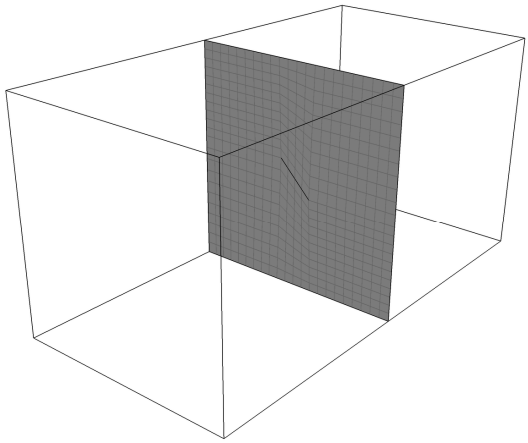

(d) Base mesh for the plate (484 cells)

Figure 9: Simple 3D case setup and meshes

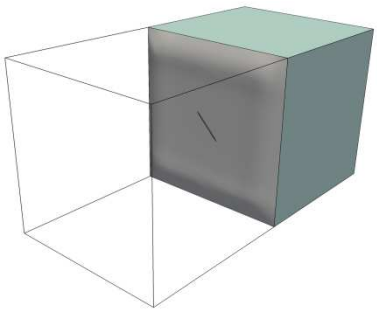

(a) Time = 2 ms

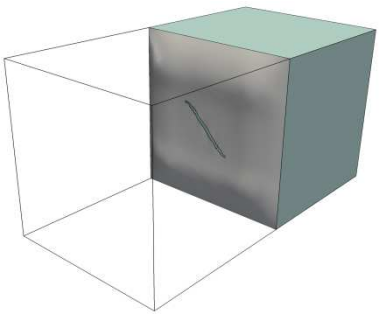

(b) Time = 3 ms

Diagonal crack propagation under the fluid pressure.

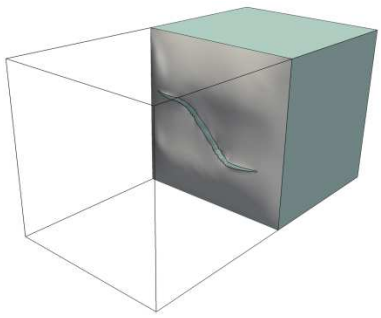

(c) Time = 4 ms

Rotation of the cracks due to the inner adaptation of the liquid pressure to the plate motion in the vicinity of the crack.

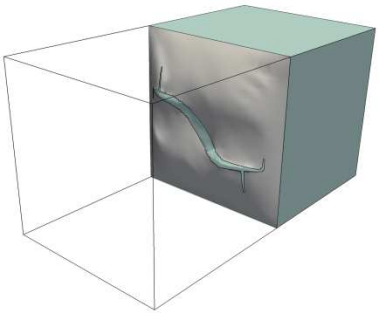

(d) Time = 5 ms

Sudden rotation and branching of the cracks close to the boundary condition.

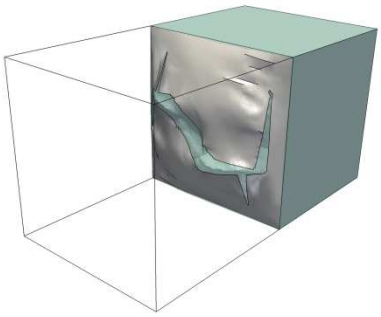

(e) Time = 7 ms

Propagation of the secondary cracks.

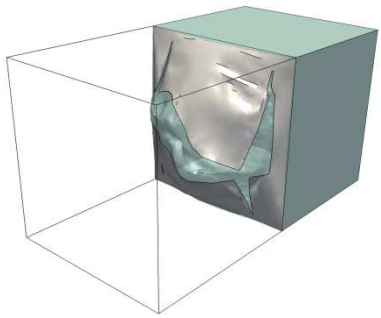

(f) Time = 10 ms

Final crack pattern almost reached. New opening mechanism in the plate and start of the main crossing liquid flow.

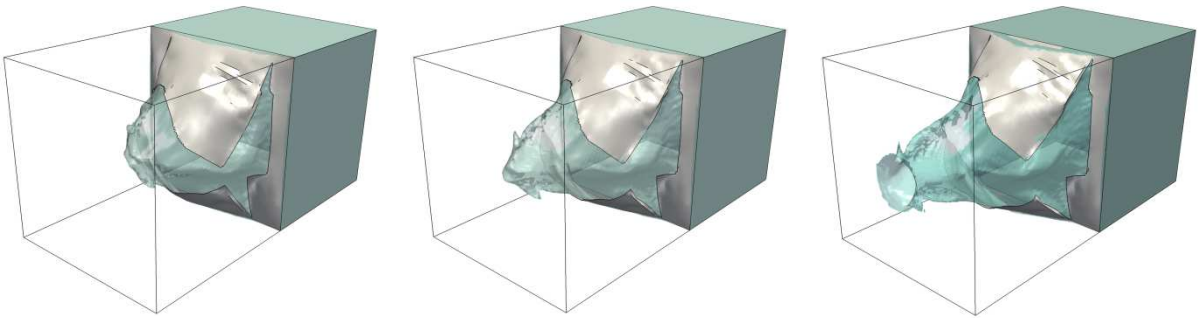

(g) Time = 15 ms (h) Time = 20 ms (i) Time = 25 ms

Development of the water jet. Water jet impacting the opposite wall of the fluid domain.

Figure 10: Description of the physical solution from Test 4 results

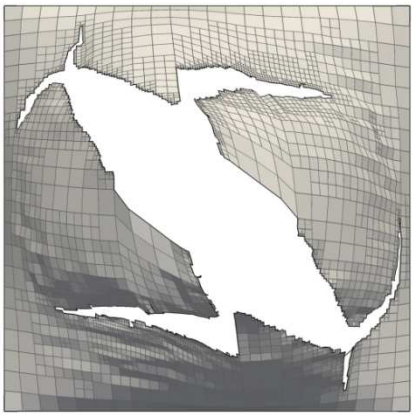

(a) Test 1: no adaptivity in the fluid

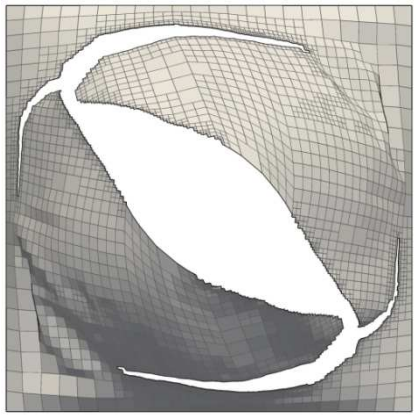

(b) Test 2: moderate adaptivity close to the structure

The representation of the fluid is too coarse to capture the pressure adaptation to the plate motion, resulting in a wrong crack pattern, quite similar to that obtained with uniform pressure on the plate in this configuration.

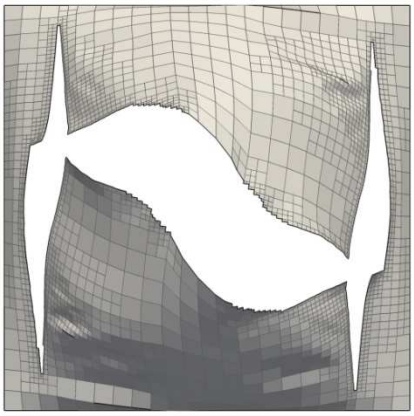

(c) Test 3: improved adaptivity close to the crack edges

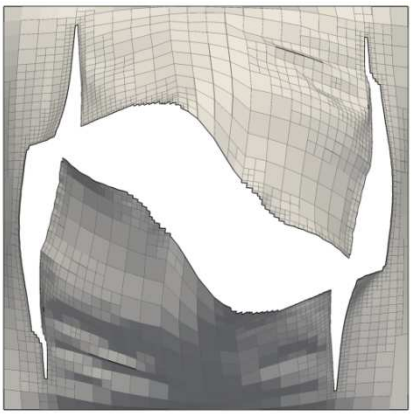

(4) Test 4: additional implementation of the VOFIRE anti-dissipative scheme for the water-air interface representation

The fluid mesh refinement in the vicinity of the crack edges allows retrieving the correct crack pattern. Adding anti-dissipation for the representation of the water-air interface brings little improvement for this topic.

Figure 11: Final crack pattern comparison for Test 1 to Test 4

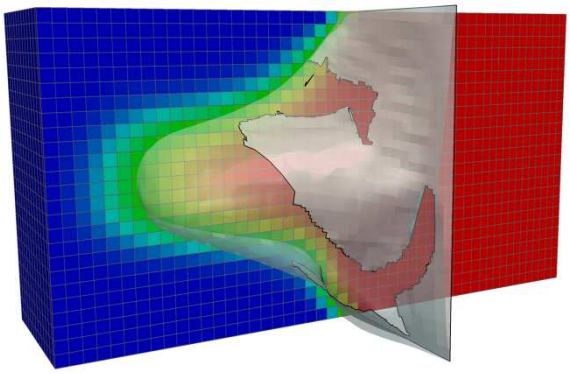

(a) Test 1

The fluid mesh is completely unable to resolve the liquid behavior close to the cracks: the velocity and pressure field are too coarse and the interface is very diffused.

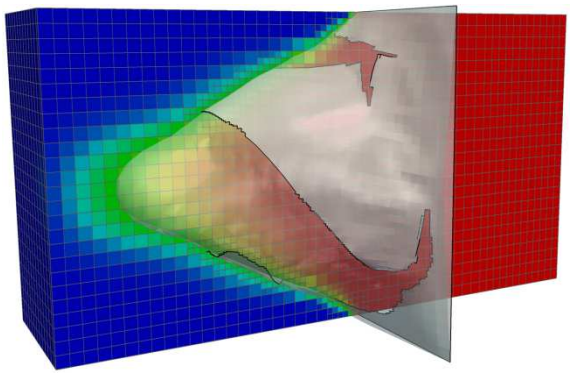

(b) Test 2

Refining the fluid mesh close to the structure improves the velocity field (and thus the pressure field) but the accuracy is still insufficient near the cracks and the interface is again very diffused.

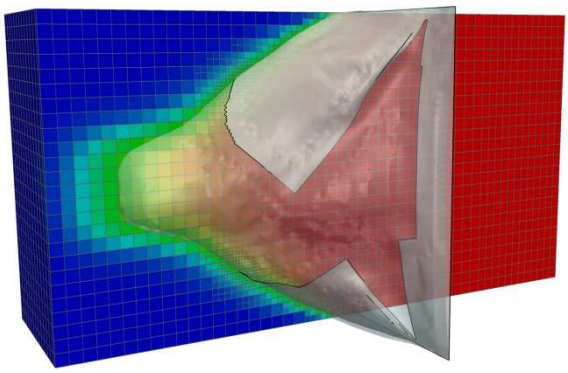

(c) Test 3

The additional refinement near the crack edges brings the needed accuracy for the velocity and pressure fields. The interface remains strongly diffused and its shape is rather coarse.

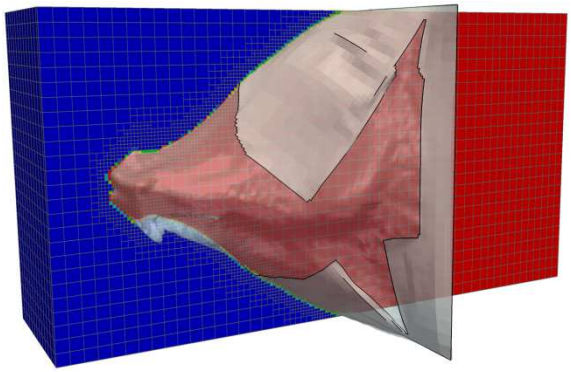

(d) Test 4

Implementing anti-dissipation with the associated mesh refinement finally provides a very significant increase of accuracy for the interface representation.

Figure 12: Interface shape comparison for Test 1 to Test 4 (field in fluid: water volumetric fraction, varying from 0 in blue to 1 in red)

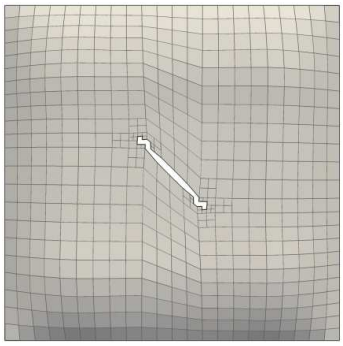

(a) Test 5, time = 3 ms

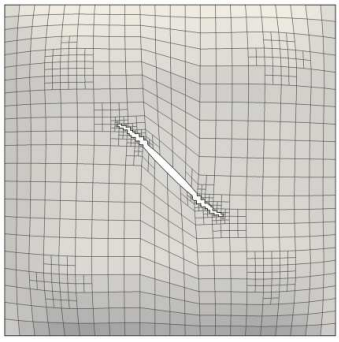

(b) Test 4, time = 3 ms

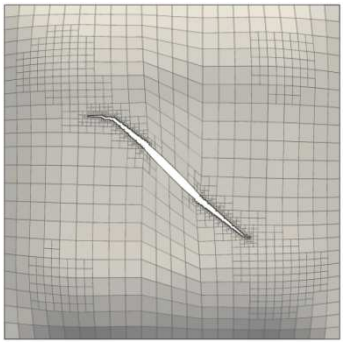

(c) Test 6, time = 3 ms

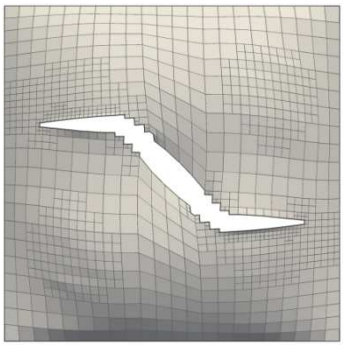

(d) Test 5, time = 5 ms

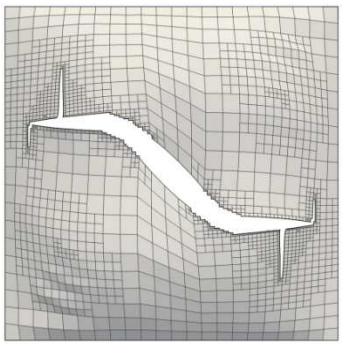

(e) Test 4, time = 5 ms

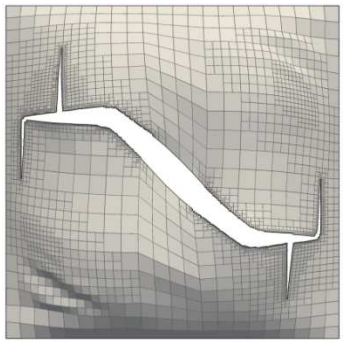

(f) Test 6, time = 5 ms

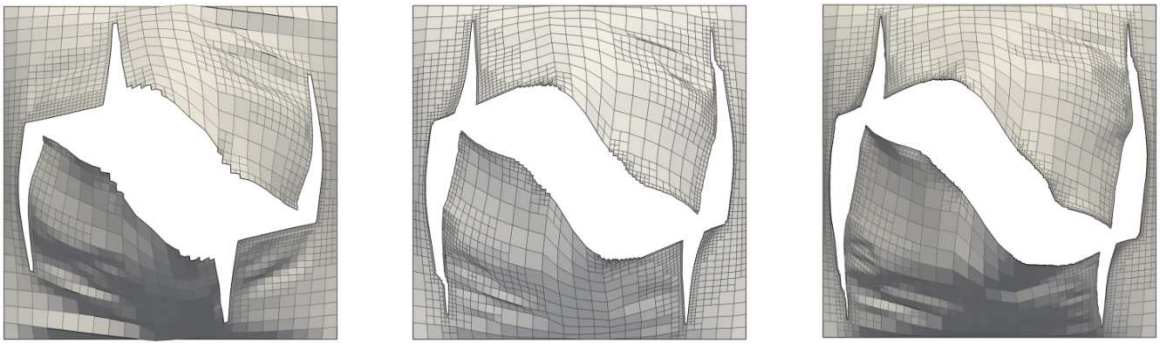

(g) Test 5, time = 10 ms (h) Test 4, time = 10 ms (i) Test 6, time = 10 ms

Figure 13: Crack propagation comparison for Test 4 to Test 6

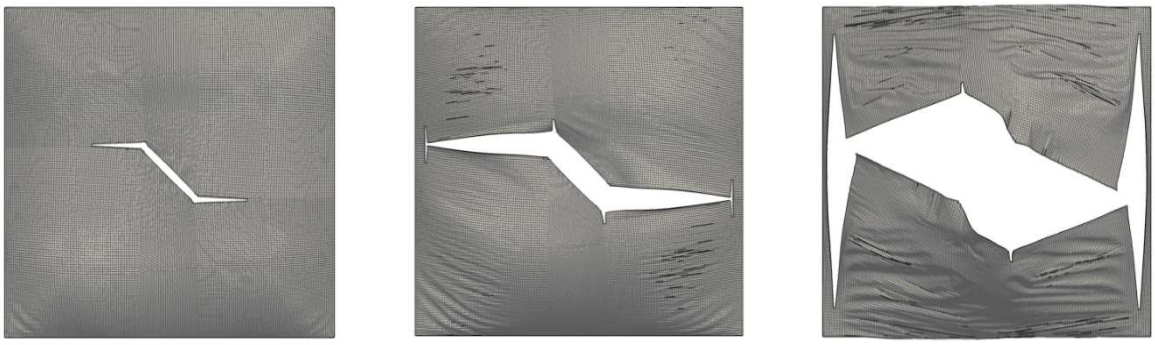

(a) Uniform refinement of plate mesh (level = 5): crack evolution at times 3, 5 and 10 ms from left to right

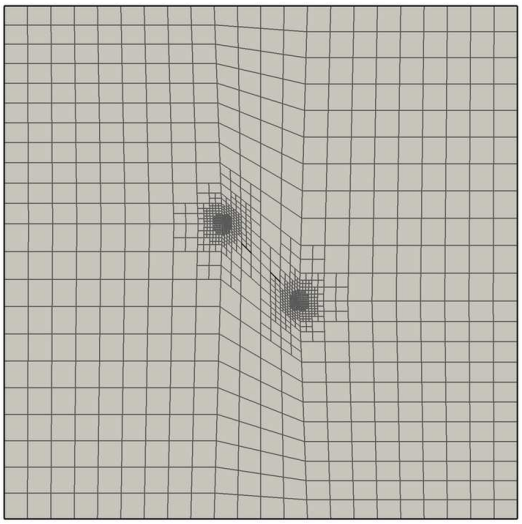

(b) Test 4 with forced initial refinement (level = 5) at crack tips

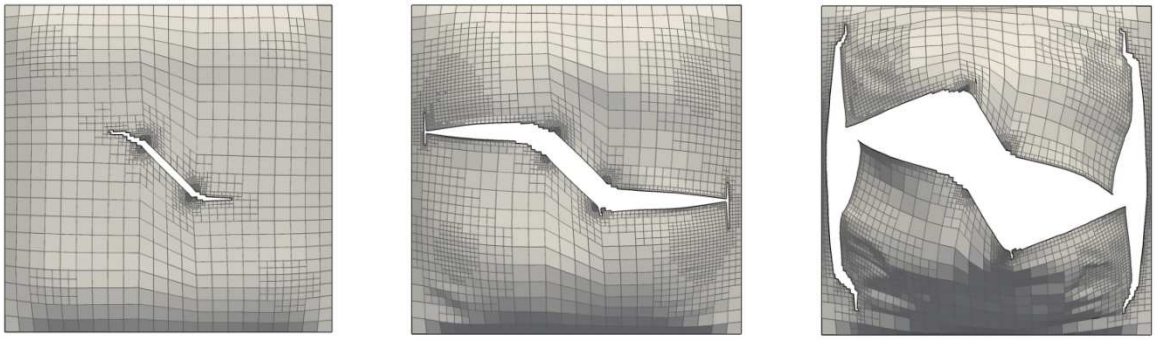

(c) Corresponding crack evolution at times 3, 5 and 10 ms from left to right

Figure 14: Crack propagation with alternate solutions for plate mesh refinement

(a) Drop tower from ONERA, Lille, France

(b) Test apparatus

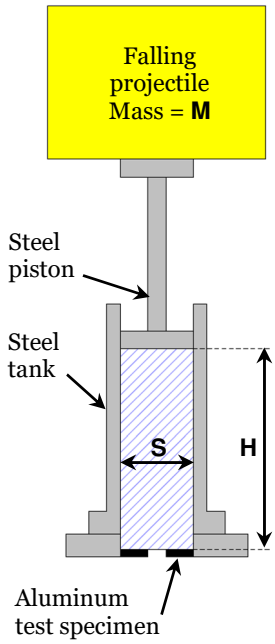

M	S	H
245 kg	8 cm	23 cm

(c) Schematics and main dimensions

Figure 15: Test bed for experimental program

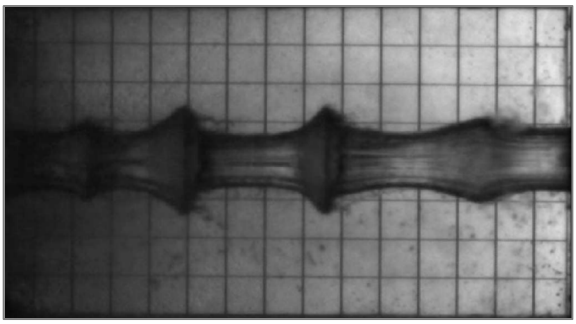

(a) View of the water jet in test E20A5 3 ms after the impact of the projectile

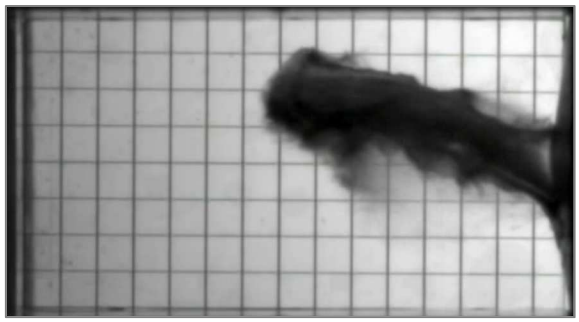

(b) View of the water jet in test FUA5 1.25 ms after the impact of the projectile

Figure 16: High-speed camera views of the water jet in Tests E20A5 and FUA5 (test specimen on the right and flow from right to left)

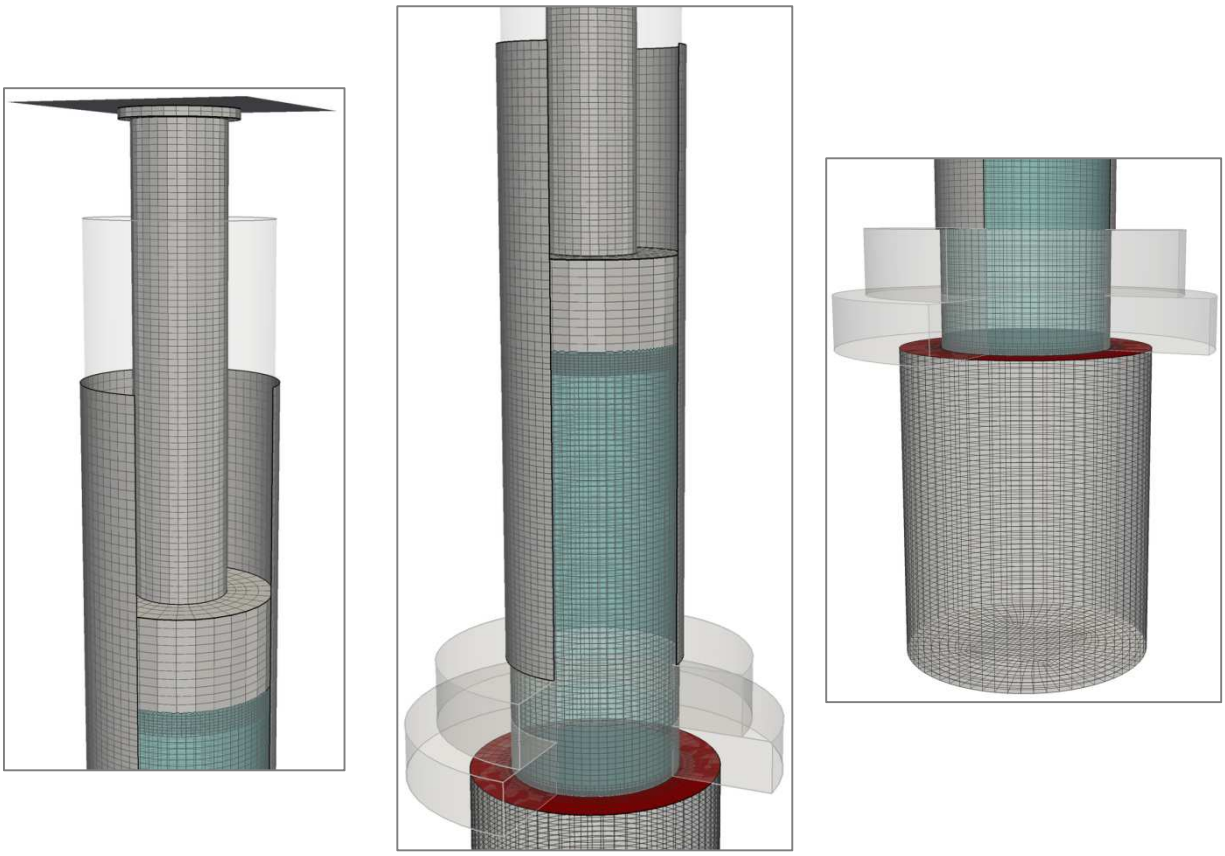

(a) Top part of the model

The projectile is modeled as a rigid plane with the correct mass and initial velocity in contact with the piston.

The fully represented piston slides inside the tank.

An air domain of arbitrary volume is modeled above the water domain.

(b) Middle part of the model

The water interacts with the bottom face of the piston and with the specimen through immersed boundary-type interfaces (thus needing the air volume above the water domain), with local mesh refinement and with the flexible part of the lateral surface of the tank through a regular conforming interface.

The massive piece at the bottom of the tank is shown (transparent) in the figure but not meshed and replaced by a rigid wall condition for the fluid.

(c) Bottom part of the model

The specimen is clamped at the distance from the axis corresponding to the actual location of the bolts connecting it to the tank.

The visualization chamber, initially filled with air, is roughly represented below the specimen. A rigid wall boundary condition is imposed on its contour (except for the portion communicating with the tank).

Figure 17: General features of all models

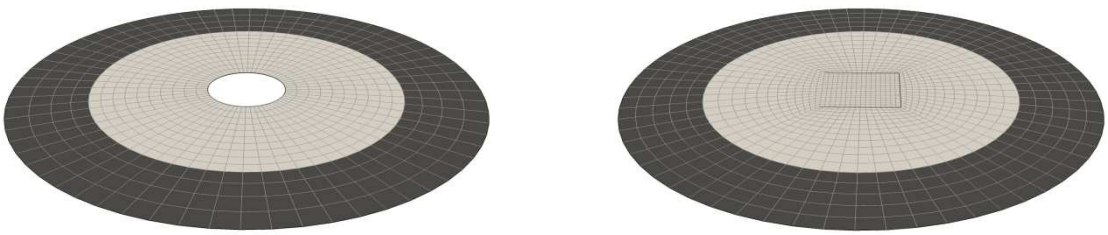

(a) Mesh of the E20A5 specimen

(b) Mesh of the FUA5 specimen

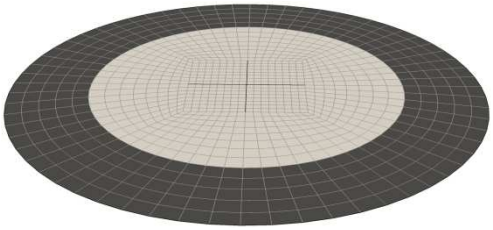

(c) Purely quadrangular mesh of the FXA5 specimen

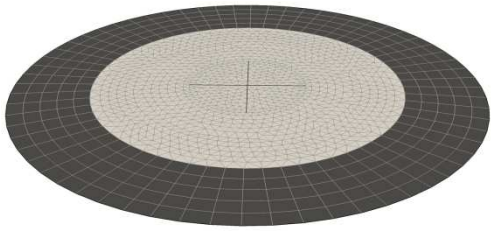

(d) Alternative mesh with triangles in the part of the FXA5 specimen in contact with water

Figure 18: Plate mesh for the specimens

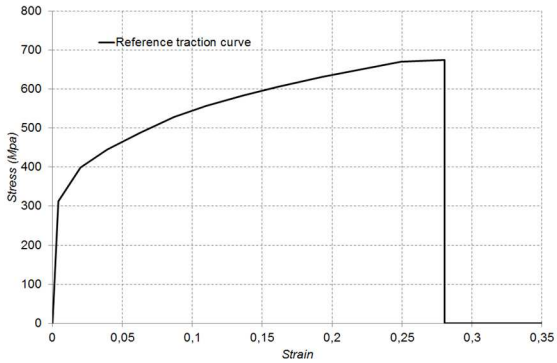

(a) Uniaxial quasi-static traction curve from Suffis, 2004

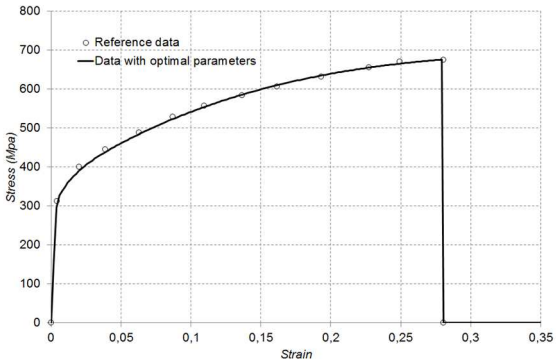

(b) Uniaxial quasi-static traction curve obtained with the proposed material model and the identified parameters

Figure 19: Identification results for the traction curve of the AU4G 2024-T4 alloy

(a) Time: 0.4 ms

(b) Time: 0.6 ms

(c) Time: 0.8 ms

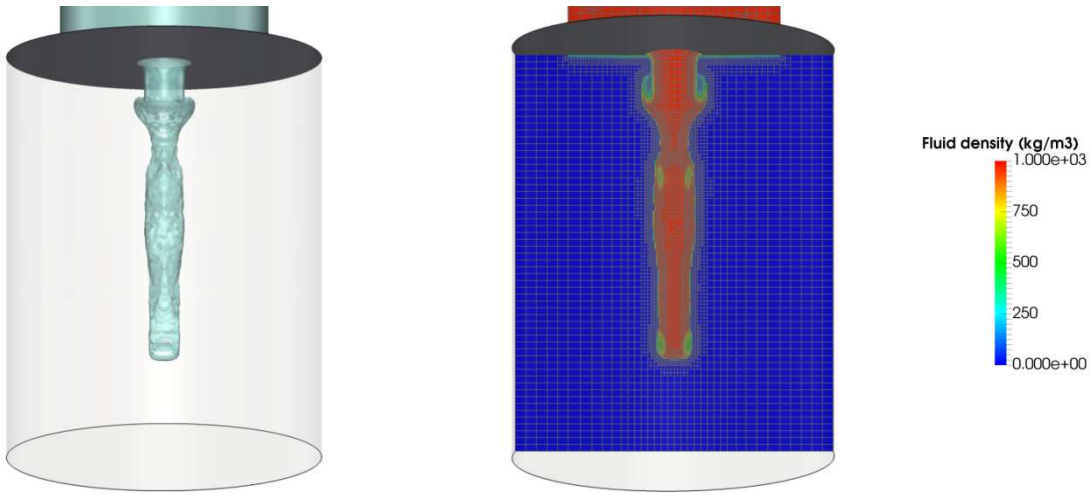

(d) Time: 1 ms (e) Mesh adaptation at after 1 ms

Figure 20: Water jet evolution up to 1 ms

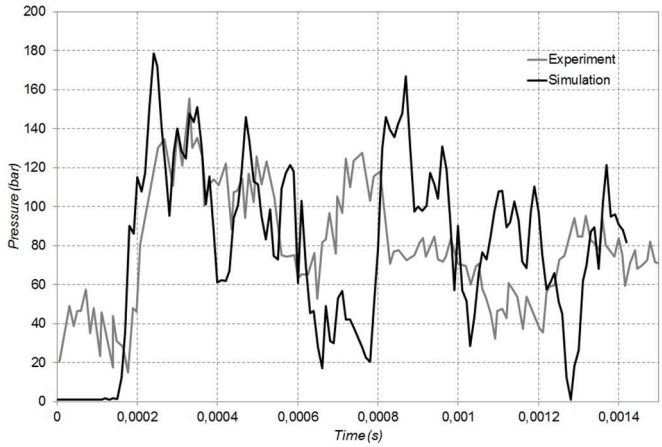

Figure 21: Internal tank pressure time history up to 1.5 ms

(a) Time: 0.6 ms (b) Time: 0.9 ms (c) Time: 1.2 ms

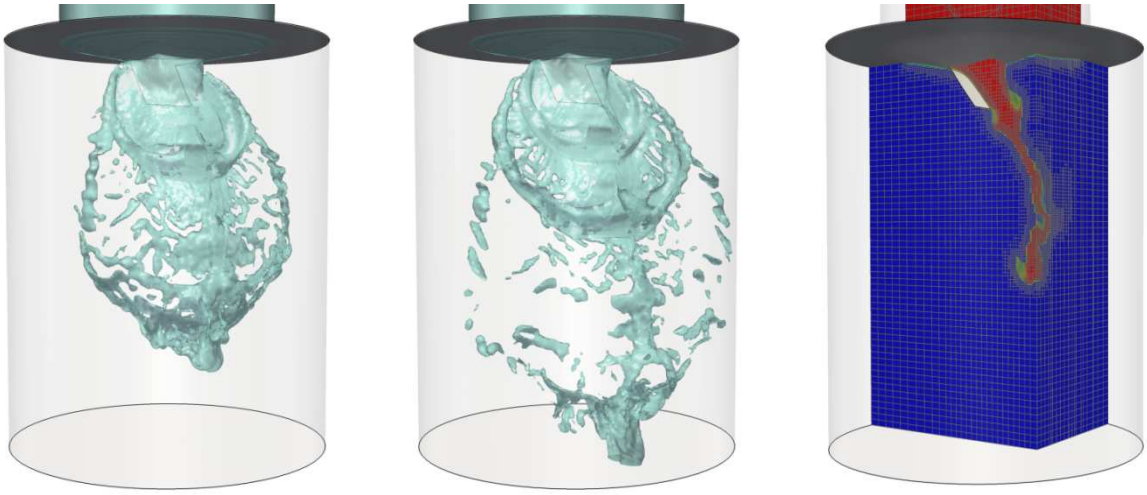

(d) Time: 1.5 ms (e) Time: 1.8 ms (e) Cut-view of fluid mesh adaptation at after 1.2 ms (same color values as in Figure 20-e)

Figure 22: Water jet evolution up to 1.8 ms

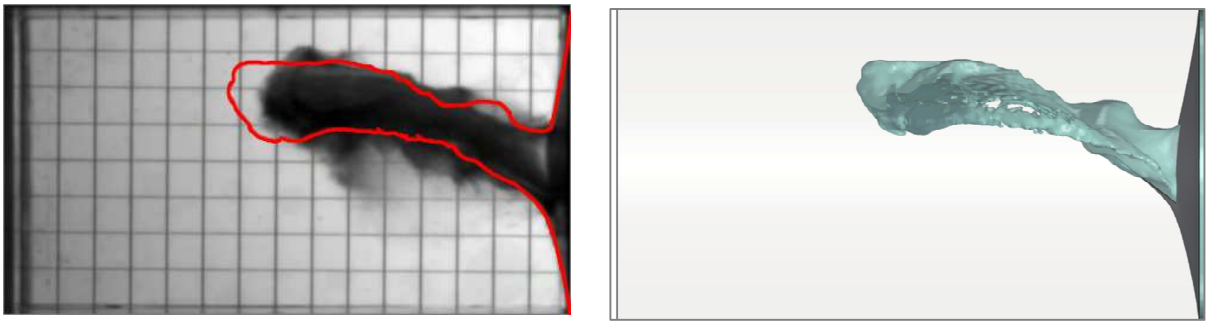

(a) Experimental reference view (the contour of the computed jet is drawn in red for quantitative comparison purposes using the same scale) (b) Simulation result

Figure 23: Water jet shapes from experiment and simulation after 1.25 ms

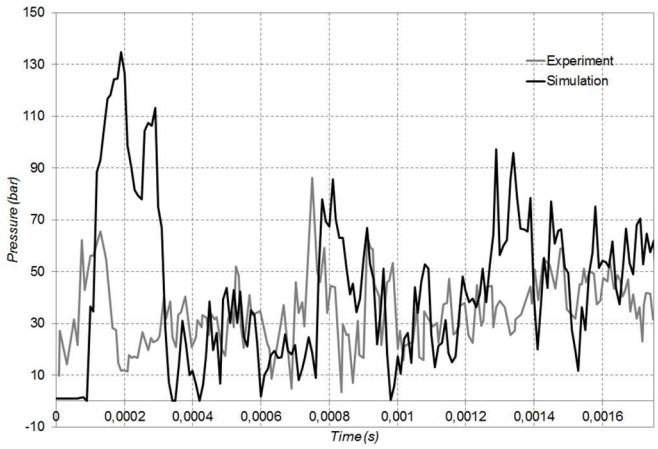

Figure 24: Internal tank pressure time history up to 1.75 ms

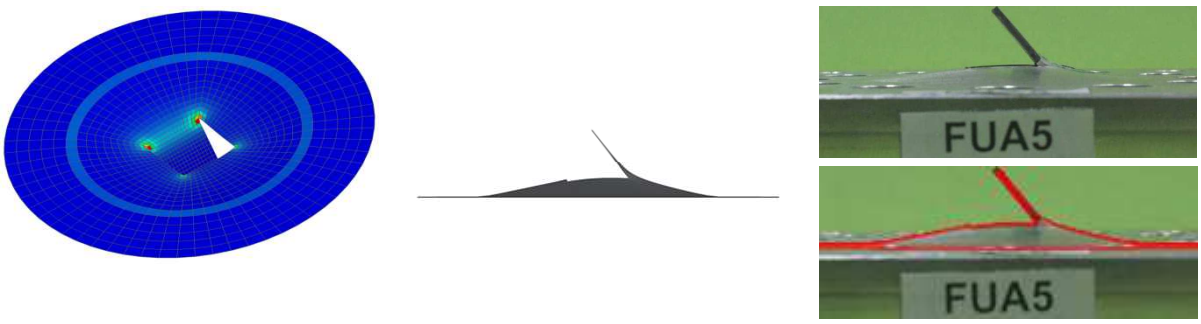

(a) Plastic strain in the specimen

(b) Permanent plate deflection and strip angle

(c) Experimental reference
Top view: actual photograph from the experiment
Bottom view: same photograph with the contour of computed deformed plate superimposed for quantitative comparison purposes

Figure 25: Permanent deformed shape of the plate

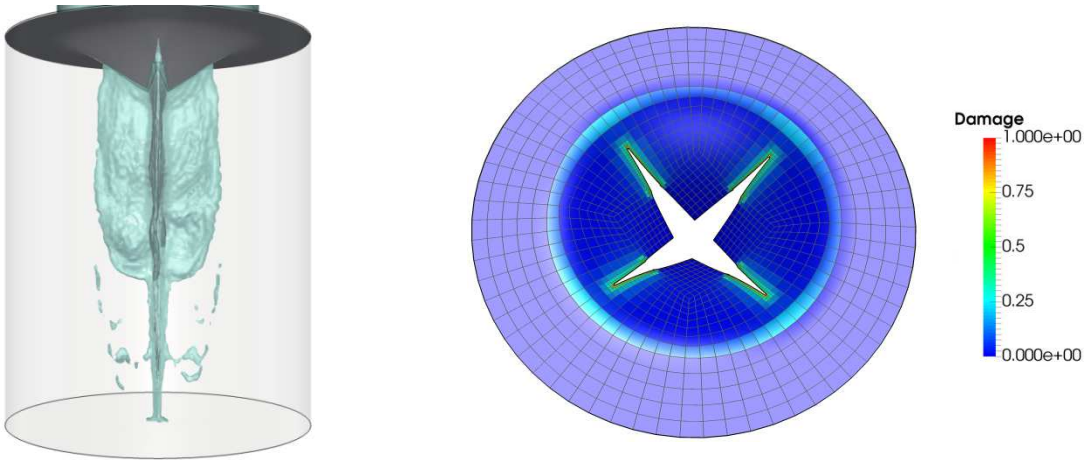

(a) Water jet shape after 2 ms

(b) Crack pattern in the specimen after 2 ms

Figure 26: Results with the purely quadrangular mesh for the specimen

(a) Time: 0.75 ms

(b) Time: 1 ms

(c) Time: 1.25 ms

(d) Time: 1.5 ms (e) Time: 1.75 ms (f) Time: 2 ms

Figure 27: Water jet evolution up to 2 ms (triangular mesh for the specimen)

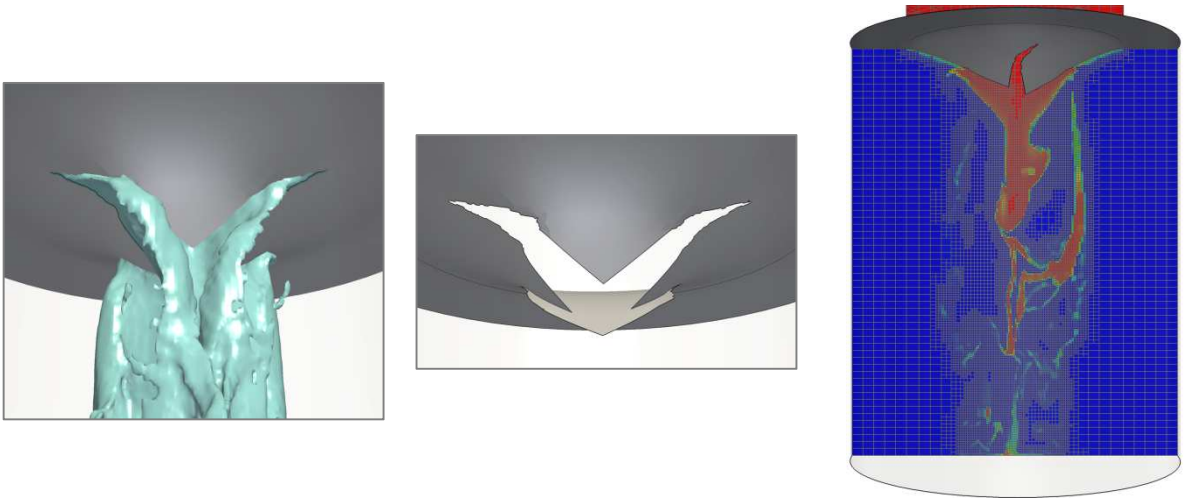

(a) Close-up view of the water flowing horizontally through curved cracks and petals with different deflections (global opening shape on the right)

(b) Fluid mesh adaptation at after 2 ms (same colorbar as in Figure 20-e)

Figure 28: Water jet interacting with the cracks in the specimen and fluid mesh adaptation

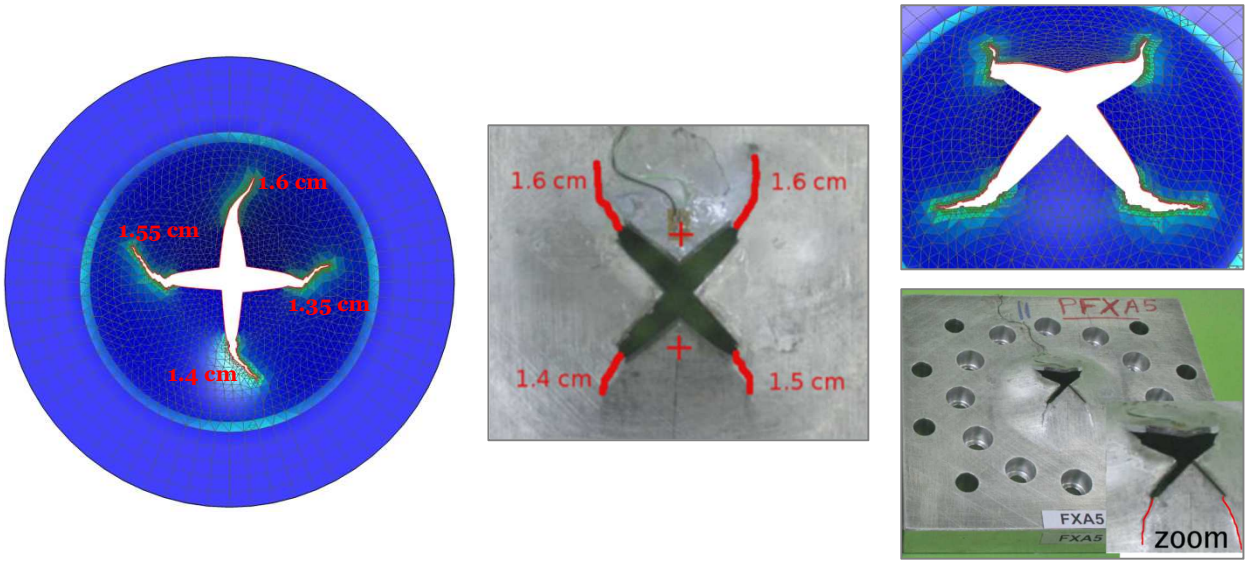

(a) Crack shapes and lengths for simulation and experiment

(b) Petals opening within the specimen for simulation and experiment

Figure 29: Comparison between simulation and experiment for crack propagation and petals opening

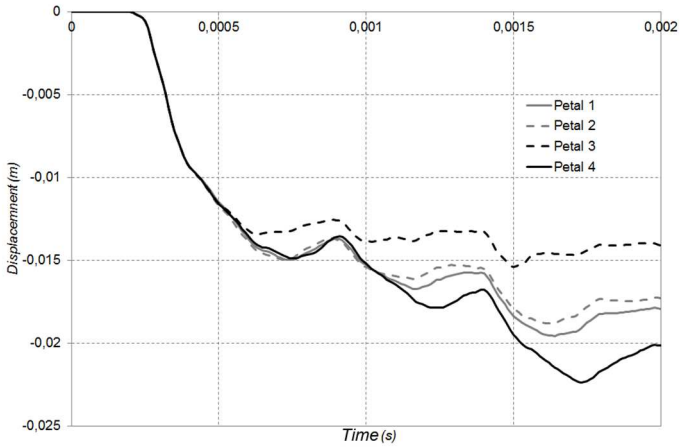

Figure 30: Vertical displacement at the tips of the structural petals